THE OXIDATION OF MATERIALS FOR INTERCONNECTS IN SOLID OXIDE FUEL CELLS

by

Julie E. Hammer

BS, University of Pittsburgh, 2002

Submitted to the Graduate Faculty of

the School of Engineering in partial fulfillment

of the requirements for the degree of

Master of Science

University of Pittsburgh

2005

UNIVERSITY OF PITTSBURGH

SCHOOL OF ENGINEERING

This thesis was presented

by

Julie E. Hammer

It was defended on

July 12, 2005

and approved by

Dr. John A. Barnard, Professor and Chairman, Department of Materials Science and Engineering

Dr. John P. Leonard, Assistant Professor, Department of Materials Science and Engineering

Dr. Gerald H. Meier, Professor, Department of Materials Science and Engineering
Thesis Advisor

Dr. Frederick S. Pettit, Professor, Department of Materials Science and Engineering
Thesis Advisor

THE OXIDATION OF MATERIALS FOR INTERCONNECTS IN SOLID OXIDE FUEL CELLS

Julie E. Hammer, MS

University of Pittsburgh, 2005

Fuel cells convert energy that is stored in a fuel to electricity and heat, and they do so with a high efficiency. As long as fuel and an oxidant gas are supplied, fuel cells can continuously produce electricity. This study focuses on materials for interconnects in solid oxide fuel cells. The interconnect is used to connect the anodes and cathodes of adjacent cells and to keep the fuel and oxidant gases separate. In this research work, ferritic stainless steels (Crofer, New Crofer, JS-3, E-brite, 26 Cr Ferritic, AL453, Modified AL453, ZMG232), an austenitic stainless steel (type 304 stainless steel), and nickel were cyclically oxidized in one hour cycles at 700^{o}C, 800^{o}C, and 900^{o}C. The atmospheres studied were simulated cathode gas (dry air), simulated moist cathode gas (air + 0.1 atm H_2O), and simulated anode gas ($Ar/H_2/H_2O$). Weight change versus time measurements and metallographic examination of the exposed alloys were used to attempt to determine the alloys most appropriate for use as interconnects. During the cyclic oxidation experiments, the sigma phase had formed in the 26 Cr Ferritic specimens at 700^{o}C in all of the studied environments. Specimens of 26 Cr Ferritic and E-brite were cyclically oxidized in dry air at 700^{o}C in 50 hour increments for 500 hours to determine when the sigma phase first appeared and the extent to which it formed. The conductivity was determined for some of the alloys that had been exposed at 900^{o}C. Not all of the alloys were tested because for the results to be accurate, a continuous oxide layer is needed, for example, no spalling could have occurred. Experiments were also performed to measure the stresses in the oxide layer of two samples of

Crofer. Both samples were cyclically oxidized at 900^{o}C for 100 hours, but one was exposed in dry air and the other was exposed in air + 0.1 atm H_2O.

TABLE OF CONTENTS

LIST OF TABLES

LIST OF FIGURES

ACKNOWLEDGMENTS

I would first like to thank Dr. Pettit and Dr. Meier for their help, advice, and expertise while both doing research for my thesis and writing it. I would also like to thank the graduate students in the high temperature group for their friendship and support, specifically Matt Stiger for his help with the stress measurements and Scot Laney for his help with the x-ray diffraction of a piece of 26 Cr Ferritic to determine if it is the sigma phase that forms. Additionally, I would like to acknowledge the work that Kelly Coyne did while completing her senior project. She performed oxidation experiments at $900^{o}C$ in dry air and air + 0.1 atm H_2O, and I have included the results of these experiments in my thesis. Also, Dr. Johnson at the National Energy Technology Laboratory (NETL) in Morgantown, West Virginia performed the conductivity experiments that have been included in my thesis. Lastly, I would like to thank my committee members, Dr. Barnard and Dr. Leonard. Financial support by NETL, Department of Energy under contract DE-FC26-02NT41578 is gratefully acknowledged.

1.0 INTRODUCTION

1.1 SOLID OXIDE FUEL CELLS

A fuel cell consists of an electrolyte with an anode (negative electrode) on one side and a cathode (positive electrode) on the other side. Gaseous fuels are continuously provided to the anode, and an oxidant is continuously provided to the cathode. An electric current is produced when the electrochemical reactions occur at the electrodes[1]. Figure 1 shows how a fuel cell operates[2]. There are many types of fuel cells, but my thesis and this section focus only on solid oxide fuel cells (SOFCs).

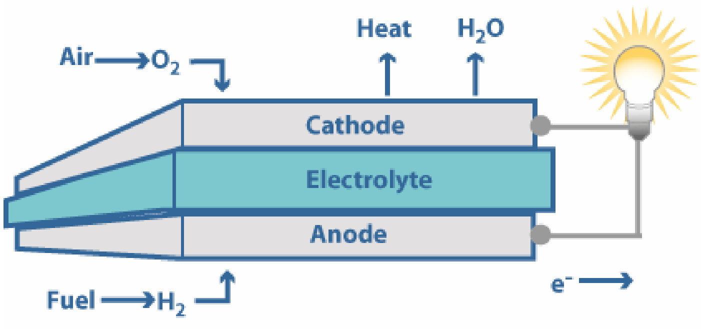

Figure 1: Conceptual Operation of a Fuel Cell

1.1.1 Components of the Solid Oxide Fuel Cell

The SOFC consists of an anode, a cathode, and a solid electrolyte. The anode is typically a nickel/YSZ (yttria stabilized zirconia) cermet, the cathode is typically a perovskite with a composition of $La_{1-x}Sr_xMnO_3$, and the electrolyte is typically YSZ[3]. In fuel cell stacks, many single cells are positioned on top of one another, and an interconnect is used to separate the individual cells (Figure 2)[4]. Interconnects can either be made of a ceramic or metal. This paper deals with metallic interconnects, mainly ferritic stainless steels, and more will be said about interconnects later.

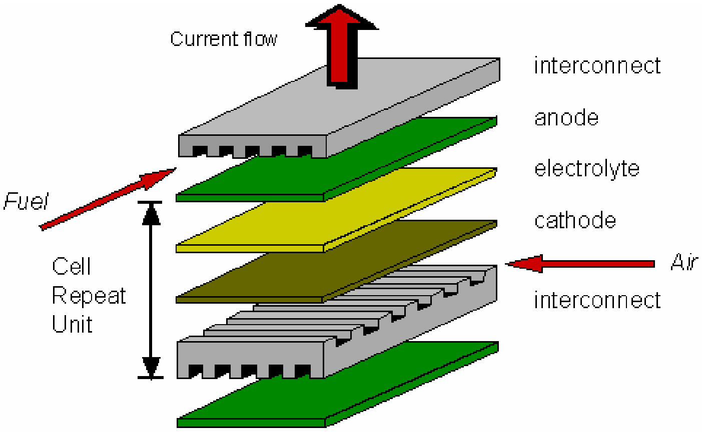

Figure 2: A schematic of a solid oxide fuel cell showing the anode, electrolyte, cathode, interconnect, and where the fuel and air enter

There are certain requirements that must be met in order for the SOFC to be functional. To reduce thermal stresses that could cause delamination and cracking during thermal cycling, components in the SOFC must have thermal expansion coefficients similar to one another. They also need to be stable in oxidizing and reducing conditions so that chemical interaction with other parts of the fuel cell is minimized. Although it is not necessary, components in a fuel cell should be easy to manufacture, have high strength and durability, and be relatively inexpensive[1].

1.1.2 Advantages and Disadvantages

The SOFC is one of the few fuel cells that has an electrolyte that is a solid, and problems with the electrolyte that some of the other types of fuel cells have are not a problem for SOFCs. For example, in some types of fuel cells, the electrolyte must by hydrated in order to operate well, and water needs to be carefully managed inside the cell[5]. This is not the case, however, for SOFCs.

SOFCs operate at a high temperature, about 600 – 1000°C. Operating at an elevated temperature allows hydrocarbon fuels to internally reform, which is a process where the fuel that is being used is converted to hydrogen inside the fuel cell. This lowers the cost because a reformer does not need to be added to the system. In addition, precious metal catalysts are not needed for high temperature operation, which also cuts down on the cost. There are disadvantages to high temperature operation as well. These are issues such as a slow startup and placing strict durability requirements on the components of the SOFC. Thermal shielding is necessary to protect personnel and keep in heat. While this is tolerable for utility applications, it is not acceptable for transportation and small portable applications[6].

Another advantage of SOFCs is their high efficiency. When converting fuel to electricity, SOFCs are estimated to be approximately 50 – 60 percent efficient. For co-generation, where the system's waste heat is captured and used, overall efficiencies could exceed 80 – 85 percent[6].

1.1.3 Applications

Stationary fuel cell systems have been put into use all over the world to provide primary power or as a backup. Currently, fuel cells have been installed in hospitals, hotels, schools, offices, and utility power plants. When fuel cells are used in large-scale buildings, energy service costs can be lowered by 20 to 40 percent when compared to conventional energy service costs.

In residential areas, fuel cells can be attached to the electric grid to supply additional power and backup assurance. In areas not reachable by power lines, fuel cells can operate as a generator for on-site service. The use of fuel cells lowers noise and air pollution. It is also possible for the heat that is given off from a fuel cell to supply space heating or hot water for a home.

Buses, airplanes, golf carts, boats, and locomotives have fuel cells that are being included in them. Fuel cell vehicles are being developed or tested by the major automotive manufacturers, and it has been thought that it will be at least 2010 before the fuel cell vehicle is commercialized.

Once they are commercially available, miniature fuel cells will be able to power cellular phones, laptops, and palm pilots for longer times than batteries can. Other applications will include video recorders and pagers, and low power devices such as smoke detectors, hearing aids, hotel locks, and burglar alarms[7].

1.2 INTERCONNECTS

In a fuel cell, the interconnect joins the anode of one cell with the cathode of a neighboring cell. It also keeps the fuel and oxidant gases separate. The following is required for the interconnect to work well:

- The thermal expansion coefficient of the interconnect must be close to that for other components in the fuel cell.
- The interconnect must be chemically stable on both the anode and cathode sides of the cell and in both reducing and oxidizing conditions.
- There must be low ionic and high electronic conductivities.
- The interconnect must be inexpensive.

Mechanical stability can also be supplied to the stack by the use of an interconnect[8].

The most often used interconnects are ceramic and metallic. In general, metallic interconnects are favored over ceramic ones for use in planar cells. Metallic materials are less brittle, easier and cheaper to fabricate, and can be more easily welded or brazed. Also, when compared to ceramics, metals and alloys have higher electrical and thermal conductivities. A high thermal conductivity leads to a temperature distribution that is consistent throughout the fuel cell stack[8].

Chromia-forming alloys are often considered as materials for interconnects. Silica and alumina offer more oxidation and corrosion protection than chromia, but in the temperature range of SOFCs, chromia has an electronic conductivity that is much higher than that for silica or alumina. Chromia-forming alloys that are based on the Co-Cr, Ni-Cr, or Ni-Fe-Cr systems have a high thermal expansion coefficient, and these alloys are not suited for use in SOFCs. Materials based on the Fe-Cr binary system are most often studied for interconnect applications in SOFCs.

In Fe-Cr alloys, an increase in the chromium content will decrease the thermal expansion coefficient[8].

1.2.1 Ferritic Steels as Materials for Interconnects

When exposed to air at temperatures between 700°C and 1000°C, steels with less than 5 percent chromium form an oxide layer that is comprised of iron oxide with chromia and/or $FeCr_2O_4$ spinel precipitates. As the chromium content of the steel increases, the oxide layers contain increasingly more chromia and spinel. A single-phase chromium oxide scale does not form until there is approximately 17 – 20 percent chromium in the alloy[8].

Titanium is added in small amounts (typically a few tenths of a percent) to provide oxidation resistance. Manganese, silicon, and aluminum are present as part of the steel making process rather than intentionally added, but they too increase the resistance to oxidation. Manganese does not have much solubility in chromium oxide, and after being exposed at an elevated temperature, it forms a chromium-manganese spinel above the chromia scale. Following exposure at a high temperature, the titanium in the steel can either form internal titania precipitates or be incorporated into the chromia scale. Because they form oxides that are more stable than chromia, both silicon and aluminum become internally oxidized instead of being incorporated into the chromium oxide layer. When the silicon or aluminum content is increased to around 1 percent, it is possible for the internal silica or alumina precipitation to change to an external silica or alumina layer. If this occurs, then the oxidation rate greatly decreases and the area specific resistance (ASR) significantly increases[8].

1.2.2 Interaction of Chromia-forming Alloys with Other Components in the Fuel Cell

In a fuel cell, the interconnect is in contact with the anode (typically a nickel/YSZ cermet). As a result, these two materials will interact with one another, and the amount and type of interaction is dependent upon the way that the interconnect and the anode are joined together. For example, good contact resistance values are initially seen if a nickel mesh is welded to a chromium-based interconnect. In this case, the contact can deteriorate over time because of interdiffusion that results in void formation due to the Kirkendall effect. If the interconnect is plated with nickel, then the deterioration of the contact becomes less of a problem. If the nickel mesh is not welded to the interconnect, but instead is in contact with the oxide layer of a chromium-based alloy, the amount of interdiffusion will be reduced. In this case, the resistivity of the chromia scale will determine the contact resistance. For a nickel mesh welded to a ferritic steel interconnect, the transport of nickel into the steel will cause austenite to form locally. The coefficient of thermal expansion and the oxidation resistance will change as a result[8].

The interconnect and the cathode (usually a La-based perovskite) are directly in contact, and compositional changes can occur as a result of the interconnect being in contact with the perovskite. The composition of the interconnect’s oxide layer and the composition of the alloy near the surface can change because of the transport of chromium into the cathode material. The oxidation resistance of the interconnect can be altered as a result of these changes. Often, a spinel layer such as $CoCr_2O_4$ or $MnCr_2O_4$ is formed between the oxide layer on the interconnect and the perovskite[8].

1.2.3 Chromium Poisoning

When oxidized at high temperatures, it is possible for chromium to vaporize from the surface of the interconnect. If this occurs, the electrical properties of a SOFC can be severely degraded. One of the proposed degradation processes is that the vaporization of chromia from the surface of the interconnect is in the form of either CrO_3 (g) or $CrO_2(OH)_2$ (g). Reduction of the vapor species occurs at the electrolyte/cathode/oxidant boundary by a reaction that forms Cr_2O_3 (s) and reacts with the cathode. The oxygen reduction that is required for SOFC operation is hindered by the formation of the Cr_2O_3 (s)[8].

If a coating such as $(La,Sr)CrO_3$ or $(La,Sr)MnO_3$ is applied to the interconnect, the amount of chromium vaporization is substantially reduced. By coating a chromium-based alloy with $La_{0.9}Sr_{0.1}CrO_3$, the chromium vaporization rate was decreased by a factor greater than 100. When compared to a chromium-based alloy with a chromia scale, uncoated iron-chromium alloys that form mixed oxide scales have a chromium vaporization rate that is reduced by factors between 2 and 23. The formation of a $(Cr,Mn)_2O_4$ scale results in the highest chromium vaporization retention values[8].

1.3 ALLOYS STUDIED

1.3.1 Crofer 22 APU

Crofer 22 APU is a high temperature ferritic stainless steel developed by ThyssenKrupp to be specifically used for interconnects in SOFCs. The chemical composition of Crofer is given below in Table 1[9].

Table 1: The composition of Crofer

Element	Typical Value (wt %)
Cr	20.0 – 24.0
Fe	balance
C	0.03 max.
Mn	0.30 – 0.80
Si	0.50 max.
Cu	0.50 max.
P	0.050 max.
Ti	0.03 – 0.20
La	0.04 – 0.20

A layer of chromium manganese oxide forms on the surface of Crofer at temperatures up to 900°C. The chromium manganese oxide layer has a high electrical conductivity and is very stable[9]. This protective oxide reduces the evaporation of chromium. The additions of lanthanum (to improve adherence) and manganese (to ensure that a chromium manganese oxide layer forms) make certain that when operation of the fuel cell begins, the chromium manganese oxide forms on the interconnect[10].

Before Crofer was developed, there had been no metallic materials suitable for use in SOFCs. It is the first alloy to be stable at high temperatures, to have low expansion, and to help prevent chromium evaporation[10]. Other characteristics of Crofer are that its oxide layer has good thermal conductivity and it resists corrosion well in both anode and cathode gases at temperatures up to 900°C[9].

Recently, modifications have been made to Crofer. This “new Crofer”, as it has been called, has silicon and aluminum levels that are kept as low as possible to reduce the amount of silica and alumina formation during high temperature exposure.

1.3.2 JS-3

JS-3 is produced by Krupp/Thyssen NIROSTA. It is a newly developed FeCrMn(La/Ti) ferritic steel for use as interconnects in SOFCs[11]. The composition of JS-3 is given in Table 2[12].

Table 2: The composition of JS-3

Element	Typical Value (wt %)
Fe	balance
Cr	23.0
Mn	0.40
Ti	0.05
La	0.10
Si	0.01 max.
Al	0.01 max.
Ni	0.002 max.
C	0.005
N	0.002
S	0.001 max.

The oxide formed upon JS-3 has a low growth rate, and a manganese chromate layer forms above the chromia scale. Because of the external spinel layer, the evaporation of chromium is greatly reduced. The oxide layers exhibit a contact resistance that is considerably lower than the contact resistance of alumina-rich scales that are often on commercial ferritic steels[11].

1.3.3 E-brite

E-brite, manufactured by Allegheny Ludlum, is a ferritic stainless steel with a body centered cubic structure. It is ferromagnetic, and it has a lower thermal expansion coefficient when compared to nickel-base alloys and austenitic stainless steels. E-brite is also resistant to oxidation and corrosion. The chemical composition can be controlled by vacuum melting techniques to assure the most favorable corrosion resistance. The composition for E-brite is shown in Table 3[13].

Table 3: The composition of E-brite

Element	Typical Value (wt %)
C	0.002
Mn	0.05
P	0.01
S	0.01
Si	0.20
Cr	26.0
Ni	0.15
Mo	1.0
N	0.010
Cu	0.02
Nb	0.10
Fe	balance

E-brite's oxidation and corrosion resistance is due to the presence of chromium, molybdenum, and niobium. When compared to conventional ferritic stainless steels, E-brite has an improved ductility and formability due to additions of carbon and nitrogen. E-brite has a high chromium content that allows a protective oxide layer to form on its surface. In addition, during thermal cycling, spallation of the protective oxide is prevented due to its low coefficient of thermal expansion. At high temperatures, there is excellent resistance to scaling because of its high chromium content and low coefficient of thermal expansion[13].

1.3.4 26 Cr Ferritic

The composition of 26 Cr Ferritic is found below in Table 4. 26 Cr Ferritic was the only alloy for which the composition was not known beforehand. It was determined by energy dispersive X-ray analysis (EDX) on the scanning electron microscope (SEM). The given composition of E-brite was compared to the composition of E-brite found using EDX, and a calculated value for the composition of 26 Cr Ferritic could be found:

$$26\,Cr\ Ferritic\ calculated = \left(\frac{E-brite\ given}{E-brite\ EDX}\right)\times\left(26\,Cr\ Ferritic\ EDX\right)$$

The only elements that were not calculated using this formula were copper, aluminum, and magnesium. Copper was not found in E-brite when the composition was determined using EDX, and aluminum and magnesium were not in the given composition of E-brite. The values of these elements are those that were obtained by using EDX on a sample of 26 Cr Ferritic. The EDX measurements are only accurate to the ones place. There are only decimals in the measurements when not having them would indicate a value of zero.

Table 4: The composition of 26 Cr Ferritic

Element	Typical Value (wt %)
Fe	balance
Cr	24
Mn	0.01
Si	0.2
Cu	6
Nb	0.1
Mo	2
Al	1
Ni	0.1
P	0.01
Mg	1

26 Cr Ferritic is an E-brite type alloy that is deoxidized by the use of silicon, which is the reason for the high silicon content. It is similar to Type 446 stainless steel and is a ferritic

stainless steel with oxidation resistance up to 2000°F (1093°C). At high temperatures, it has a low strength, which limits its use[14].

1.3.5 AL453

AL453 is an iron-chromium ferritic stainless steel that is produced by Allegheny Ludlum. It is a single phase alloy and small amounts of rare earth metals (REM) have been added, which decrease the possibility of spallation at increased temperatures. The composition of AL453 is shown in Table 5[15].

Table 5: The composition of AL453

Element	Typical Value (wt %)
C	0.03
Mn	0.3
P	0.02
S	0.030 max.
Si	0.3
Cr	22.0
Ni	0.3
Ti	0.02
Al	0.6
REM (Ce + La)	0.10 max.
Fe	balance

The rare earth metals are added as a combination of cerium and lanthanum in a ratio of 2:1. There are other REM additions in AL453, but they are present in lesser amounts. The chromium content of AL453 is higher than that of the more common ferritic stainless steels. As a result, AL453 is an alloy that is highly resistant to oxidation. A small amount of mischmetal, which is the source of the cerium and lanthanum, is added to improve upon the oxidation resistance, taking advantage of what is called the reactive element effect. This effect occurs when trace amounts of rare earth elements are added to an alloy that forms a chromium oxide layer. The REM additions increase the oxidation resistance by lowering the oxide scale growth rate[15].

During thermal cycling, a large amount of stress can be generated in the oxide scale, and it is possible for spallation to occur. Once this happens, the metal may quickly be consumed. The coefficient of thermal expansion of AL453 is less than that of austenitic stainless steels, and it therefore has a higher resistance to spallation. This is because during the expansion and contraction from thermal cycling, there is an improved compatibility between the scale and substrate. The reactive element effect significantly strengthens the scale/metal interface, which also improves the spallation resistance of AL453[15].

1.3.6 Modified AL453

Modified AL453 has the same composition as the AL453 mentioned above, but a special processing technique has been used to improve the oxidation resistance[16]. First, the AL453 was mechanically polished. It was then placed into an acid bath, where it was treated electrochemically[17]. The resistance to oxidation may be decreased if the surface is disrupted before use[16].

1.3.7 ZMG232

ZMG232 has been developed by Hitachi Metals to meet the requirements for SOFC applications. This alloy is a ferritic stainless steel with 22 percent chromium and various other elements added[18]. The composition of ZMG232 is given in Table 6[19].

Table 6: The composition of ZMG232

Element	Typical Value (wt %)
Fe	balance
Cr	22.0
C	0.02
Mn	0.50
Si	0.40
Ni	0.26
Al	0.21
Zr	0.22
La	0.04

The thermal expansion coefficient of ZMG232 is similar to that of YSZ, which is the electrolyte for SOFCs. Additionally, ZMG232 exhibits excellent oxidation resistance after exposure at elevated temperatures and for extended periods of time. This alloy also has a conductivity that is high enough for it to be used as an interconnect[18].

1.3.8 Nickel

Nickel is a metal with good high temperature oxidation and corrosion resistance and exceptional strength when properly alloyed[20, 21]. It also has many significant magnetic properties[20]. It is tough and ductile due to its crystal structure which is face centered cubic. Nickel is relatively expensive, and even though there are only a small number of metals that have similar properties, it has limited uses because of its high cost[21].

Nickel that is commercially pure has a nickel content of about 99.5% and also contains cobalt, carbon, and small amounts of other elements. It is corrosion resistant in many environments and has good mechanical properties. Much of its strength is retained at high temperatures, and at low temperatures, it is tough and ductile[21].

1.3.9 Type 304 Stainless Steel

Austenitic stainless steels are used in applications where alloys are needed that exhibit resistance to oxidation and corrosion, have high strength and low weight, and are easy to fabricate. Type 304 stainless steel is the most commonly used austenitic stainless steel[21]. It has a face centered cubic structure and is nonmagnetic in the annealed condition[22]. The composition of Type 304 stainless steel is shown in Table 7[23].

Table 7: The composition of Type 304 Stainless Steel

Element	Typical Value (wt %)
Fe	balance
C	0.08 max.
Mn	2.0 max.
P	0.045 max.
S	0.030 max.
Si	0.75 max.
Cr	18.0 – 20.0
Ni	8.0 – 10.5
N	0.10 max.

Type 304 stainless steel is corrosion resistant in many types of environments. Resistance to oxidizing atmospheres is given by its chromium content (18 to 20 percent), and resistance to reducing environments is provided partly by the amount of nickel (8 to 10.5 percent)[23]. Its low carbon content provides an increase in corrosion resistance over other types of stainless steels[22].

1.4 OXIDATION

1.4.1 Oxidation of Metals

Because they are unstable in environments that are oxidizing, most metals will react and form an oxide layer on their surface. The rate at which this occurs is dependent upon many factors, including the manner of transport in the oxide scale and the whether the reactant phases can remain physically continuous. The phases that form and the order in which they do so is determined by the thermodynamic driving forces for the reactions[24]. Considering the equation

$$M(s) + \tfrac{1}{2}O_2(g) = MO(s)$$

the reactants will separate into the reaction product MO as shown in Figure 3.

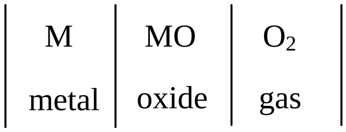

Figure 3: Separation of $M(s) + \tfrac{1}{2}O_2(g) = MO(s)$ into metal, oxide, and gas components

If the reaction is to continue, it is necessary for one of the following to occur:

1) Oxygen is transferred through the oxide to the oxide/metal interface, and it reacts there.

2) Metal is taken through the oxide to the oxide/gas interface, and the reaction occurs there[25].

When high purity nickel is oxidized, it forms a single layer oxide scale consisting of NiO that adheres well to the surface and is compact. The placement of platinum markers on the surface of the metal before reaction helps to determine if the oxide forms by outward cation migration or inward anion migration. After the oxidation of nickel, platinum markers were found at the oxide/metal interface, signifying that the oxide scale grows by the outward migration of nickel[25].

An oxide scale consisting of two layers is formed on nickel that contains 0.1% impurities. Both layers are NiO, but the outer layer is compact and the inner layer is porous. A platinum marker experiment was performed with the less pure nickel, and after oxidation, they were found at the interface between the outer and inner layers of the NiO. Outward nickel migration is responsible for the growth of the outer layer, and the inner layer is grown by inward oxygen migration[25].

1.4.2 Oxidation of Alloys

It is possible for the oxidation of alloys to be more complicated than the oxidation of metals because of some of the following reasons:

- By changing the composition, new oxide scales may form that contain more than one cation and that are different than what would form if the metal were pure. The possible effects from oxide layers that have more than one cation include a change in the transport of ions within the oxide because of different ion mobilities in the new scale and vaporization of the new oxide layers.

- The oxide scale adherence to the surface of the alloy can be altered by the formation of new phases and changes in composition.
- It is possible for the oxide to grow and consume one of the metals over the others. If this occurs, a concentration gradient may exist in the alloy[26].

Iron-chromium alloys that contain small amounts of chromium form iron oxides and chromium-rich oxides on the surface. $FeCr_2O_4$ islands form within the FeO layer. These alloys do not contain an internal oxidation zone because the external oxide scale grows quickly enough that the internal oxidation zone thickness is negligible in comparison. As the chromium content is increased, the layer of FeO becomes thinner due to the hindrance of Fe^{2+} ions by the islands of $FeCr_2O_4$. If the amount of chromium is further increased, a spinel of $Fe(Fe,Cr)_2O_4$ forms on the surface. After an extended amount of time, the outer surface of the oxide scale will consist of high purity iron oxides. This is because, in the $Fe(Fe,Cr)_2O_4$ spinel, iron ions are more mobile than Cr^{3+} ions. When the chromium content reaches approximately 20%, Cr_2O_3 will initially form on the surface. If the alloy contains more than this amount of chromium, then an oxide scale that is permanent and protective will develop[25].

1.5 SIGMA PHASE

Stainless steels contain at least 12 percent chromium in order to make the steel “stainless”. This amount of chromium is enough to form a chromium oxide layer on the surface of the steel to protect it from corroding. Because chromium is such a significant alloying addition in stainless steels, the iron-chromium phase diagram (Figure 4) is important.

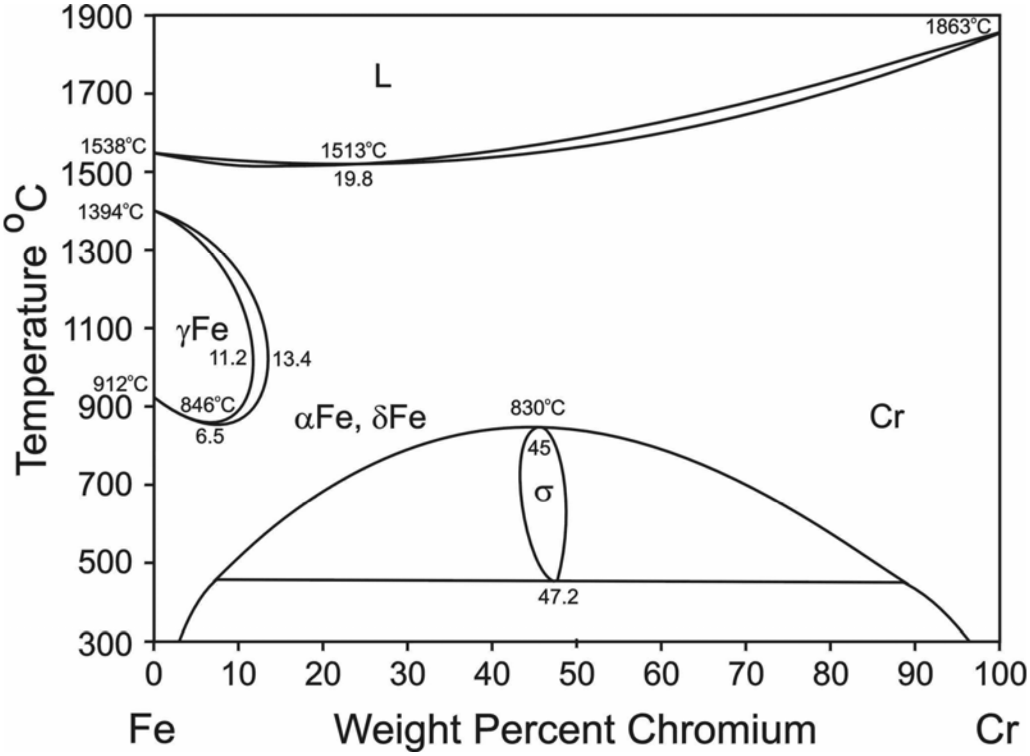

Figure 4: The Fe-Cr Phase Diagram

At temperatures below 830°C and around 45 weight percent chromium, an intermediate phase is formed called the sigma (σ) phase, which is hard and brittle. In order to form this phase, very slow cooling rates through the regions on the phase diagram where sigma can form or prolonged aging in these same areas is necessary[21]. The crystal structure of the sigma phase is tetragonal with a c/a ratio of 0.52, and there are 30 atoms in the unit cell. At room temperature, embrittlement as a result of the sigma phase is at its greatest[27].

As a general rule, the formation of the sigma phase is promoted by any element that stabilizes ferrite. Increasing the amount of chromium will also increase sigma formation. Even in small amounts, silicon and molybdenum will noticeably accelerate the formation of sigma. Aluminum has the same effect, but to a lesser extent. Nickel and manganese in small amounts will increase the rate of sigma phase formation. Large amounts of these two elements stabilize austenite and will slow down sigma formation. The addition of carbon causes chromium carbides to form, which lowers the amount of chromium in solid solution and reduces the formation of the sigma phase[27].

1.6 DUAL ATMOSPHERE

Interconnects are simultaneously exposed to an oxidizing atmosphere (air) on one side and a reducing atmosphere (fuel) on the other. It is therefore necessary for an interconnect to be stabile in a dual environment. Many recent studies though have been performed using either an oxidizing environment or a reducing environment, assuming that the oxide scale growth and corrosion behavior is the same for a single atmosphere and a dual atmosphere. However, this is not the case. It has been discovered that for ferritic stainless steels, the scale growth and composition of the air side after exposure to a dual air/hydrogen atmosphere considerably differs from what is observed if exposed to air on both sides[28, 29].

1.6.1 Oxidation Behavior under Dual Atmosphere Conditions

To study the oxidation behavior of ferritic stainless steels under dual atmosphere conditions, one sample of Crofer had been exposed to air on both sides and another sample had been exposed to air on one side and moist hydrogen (containing approximately 3% H_2O) on the other side. In this study, both samples were oxidized isothermally for 300 hours at 800^oC. X-ray diffraction (XRD) analysis was performed on the oxide scales grown on the two samples of Crofer. Shown in Figure 5[29] are the XRD patterns from this analysis, which showed that Cr_2O_3 and M_3O_4 spinel (M is Cr, Mn, and/or Fe) have formed on both samples. Based only on XRD information, the chemistry of the spinel phase cannot accurately be determined because of the similarity in size of Cr, Mn, and Fe. According to the peak intensity ratios, the ratio of the weight of spinel to the weight of chromia was higher for the air side of the dual atmosphere sample. Use of the SEM showed a homogeneous microstructure of the surface of the single atmosphere sample. Chemical and microstructural analyses of the cross section of the oxide formed during exposure to air on both sides signified that a manganese-rich M_3O_4 layer formed above a chromia layer. Iron was not found in the spinel and chromia layers. For Crofer exposed in the dual atmosphere environment, analysis on the SEM indicated coarse spinel crystallites embedded in a microstructure otherwise similar to that of the single atmosphere sample. The oxide on the air side of the Crofer that was exposed to air and moist hydrogen had a similar layered structure and thickness to that which was exposed only to air. In the oxide layer of the sample exposed to dual atmospheres, a substantial amount of iron was discovered. The iron was found mostly in the spinel in the form of $(Mn, Cr, Fe)_3O_4$ on the air side of the dual atmosphere sample[29].

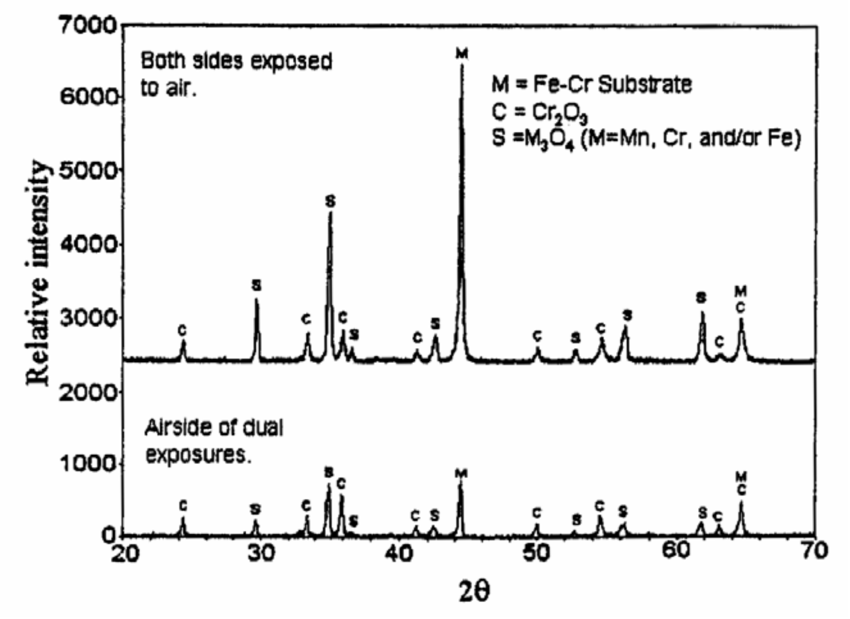

Figure 5: XRD pattern comparing the scale on the air side of the Crofer sample that had been exposed to dual atmospheres to the Crofer sample that had been exposed to air on both sides. Samples were isothermally oxidized.

A sample of Crofer was isothermally exposed to moist hydrogen on both sides at 800°C for 300 hours. A comparison was made to the fuel side of a dual exposure sample. Figure 6[29] shows the XRD pattern of the fuel side of the sample exposed in the dual atmosphere environment and the pattern from the sample exposed to fuel on both sides. These patterns show that the oxides formed on both samples are Cr_2O_3 and M_3O_4 spinel (M is Cr, Mn, and/or Fe). The spinel to chromia weight ratios were similar in the scales grown on both the sample exposed to fuel only and the fuel side of the sample exposed to dual environments. SEM analysis of the oxide scale on the fuel only sample revealed a fibrous phase, which was rich in magnesium and chromium and thought to be the spinel phase, surrounded by a fine substrate, which was rich in chromium. Cross-sectional analysis established that the scale contained a top layer that was rich in spinel and a sublayer that was rich in chromia. There was also a large amount of porosity in the oxide layers. The fuel side of the sample exposed to dual atmosphere conditions had a scale similar to that which was formed in fuel only, with the only difference being that there was a less developed spinel fiber phase. The oxide scale consisted of a layered structure similar to the layers that grew on the fuel only sample. The fuel side of the sample exposed to dual atmospheres contained a small amount of porosity[29].

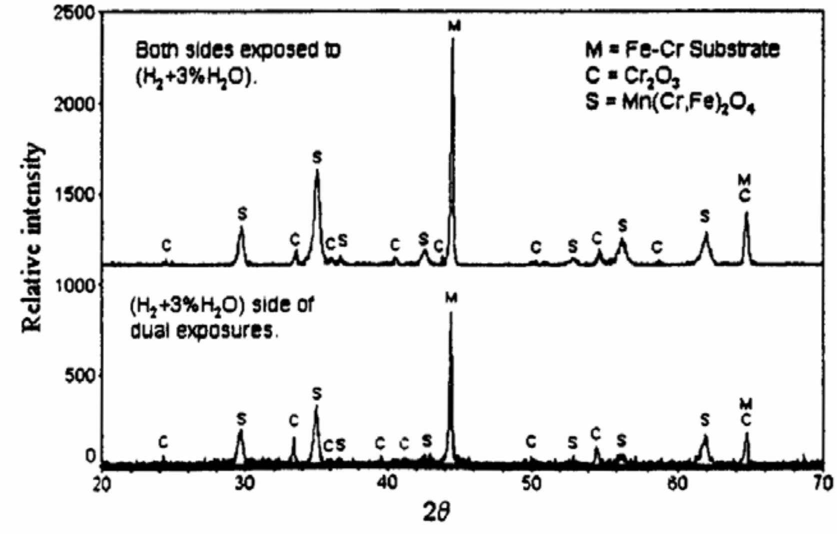

Figure 6: XRD pattern comparing the scale on the moist hydrogen (fuel) side of the Crofer sample that had been exposed to dual atmospheres to the Crofer sample that had been exposed to fuel on both sides. Samples were isothermally oxidized.

1.6.2 Thermal Cycling Effects due to Dual Atmosphere Conditions

Cyclic oxidation experiments were carried out to determine what effects this would have on dual atmosphere samples. In this study, the tests were performed by heating the samples to 800°C and holding at this temperature for 100 hours. The samples were then cooled to room temperature. They were then heated, held at temperature for 100 hours, and cooled to room temperature twice more, for a total of 3 cycles. One sample of Crofer had been oxidized under dual atmosphere conditions, and another sample had been oxidized in air only. The XRD patterns from the air side of the sample exposed to dual environments and from the sample exposed to air only are shown in Figure 7[29]. It was found that the scale on the sample exposed only to air consisted of chromia and M_3O_4 spinel (M is Cr, Mn, and/or Fe), and the scale on the air side of the dual atmosphere sample consisted of chromia, spinel, and hematite (Fe_2O_3). SEM analysis of the scale on the air only sample revealed a smooth homogeneous microstructure. It was established that the scale contained two layers, a manganese and chromium rich top layer and a chromium rich bottom layer. A significant difference was found with the air side of dual atmosphere sample. The surface of the scale consisted of randomly distributed nodules that were rich in iron. After exposure at 800^{o}C for three cycles (300 hours total exposure time), the nodules developed until they were about two to three times the thickness of the chromia scale. Penetration of the chromia into the metal substrate was increased in the areas where the iron-rich nodules were found. This was because, in these areas, there was metal loss from the metallic elements that were consumed. The nodules were found to contain mostly iron near the top and mostly chromium and manganese in the bottom parts. Chemical analysis found 32% iron at the top of a nodule, and the bottom of the nodules has a composition similar to that of an oxide scale that had formed in a region without nodules. Iron was also usually found in the top part of the scales grown in the nodule-free areas[29].

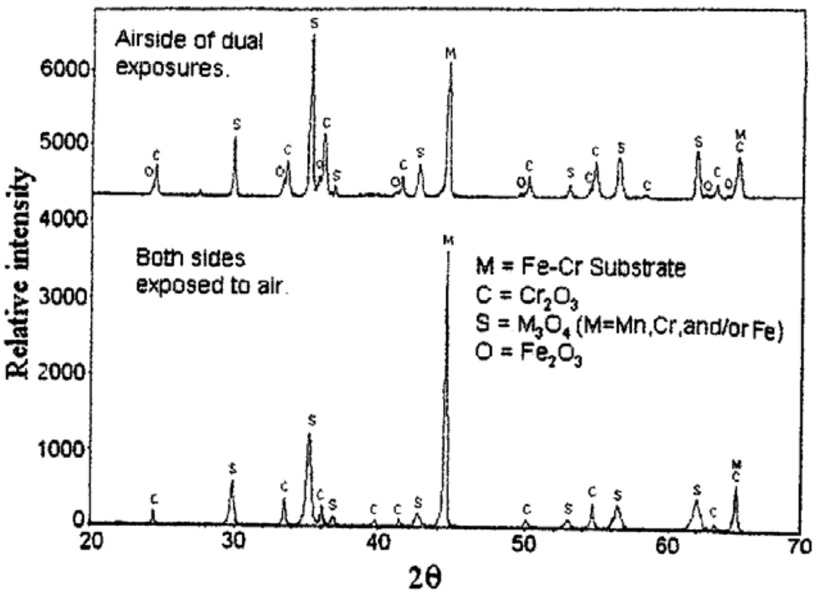

Figure 7: XRD pattern comparing the scale on the air side of the Crofer sample that had been exposed to dual atmospheres to the Crofer sample that had been exposed to air on both sides. Samples were cyclically oxidized.

A comparison was made between the fuel side of a sample of Crofer that had been cyclically oxidized under dual atmosphere conditions, and another sample that had been cyclically oxidized in fuel only. The cyclic oxidation experiments were performed the same way as described above. The microstructure and composition of the fuel side of the sample exposed to dual atmospheres were similar to those for the sample exposed to fuel only. Microstructural and chemical analyses showed that the scales of both samples (the fuel side of the dual environment sample and the sample exposed to fuel only) consisted of chromia and M_3O_4 (M is Cr, Mn, and/or Fe). Additionally, the top layers of the oxide scales on both samples did not contain iron[29].

2.0 PROCEDURE

2.1 OXIDATION

Samples of various types of stainless steels and pure nickel were polished to a 600 grit finish. The materials used were Crofer, New Crofer, JS-3, E-brite, 26 Cr Ferritic, AL453, Modified AL453, ZMG232, Ni, and Type 304 stainless steel (see section 1.3 for the compositions of the alloys). The specimens were then exposed for one hour cycles (45 minutes hot time, 15 minutes cold time) at 700^oC, 800^oC, or 900^oC. Atmospheres that were studied were dry air (simulated cathode gas), air + 0.1 atm H_2O (simulated moist cathode gas), and $Ar/H_2/H_2O$ (simulated anode gas). The $Ar/H_2/H_2O$ atmosphere had an oxygen partial pressure of 10^{-17} atm for 900°C and 10^{-20} atm for 700°C. The furnaces that were used for the exposures are shown in Figure 8 (for dry air), Figure 9 (for air + 0.1 atm H_2O), and Figure 10 (for $Ar/H_2/H_2O$).

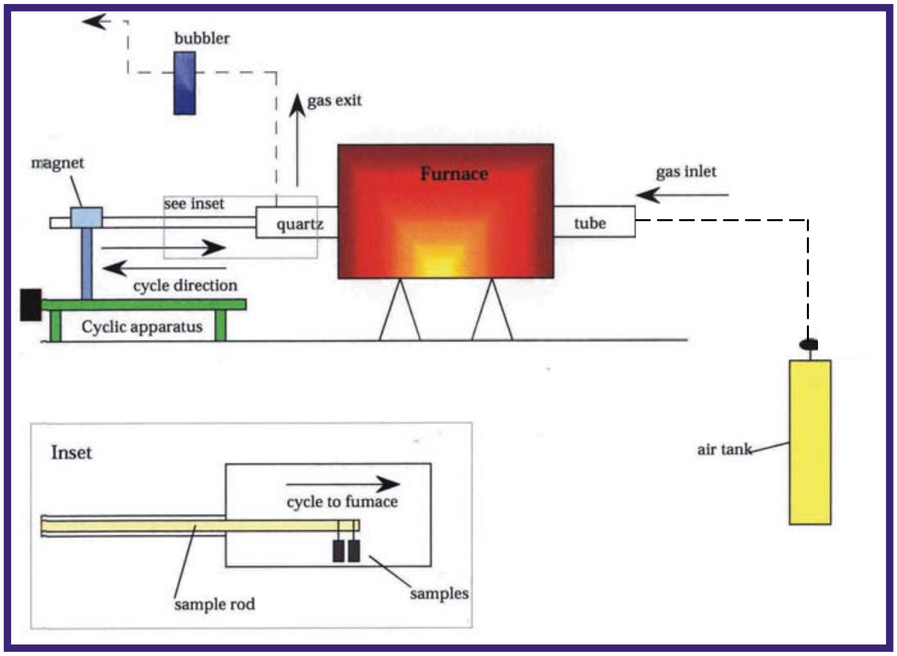

Figure 8: Schematic diagram of the apparatus used for cyclic oxidation exposures with dry air

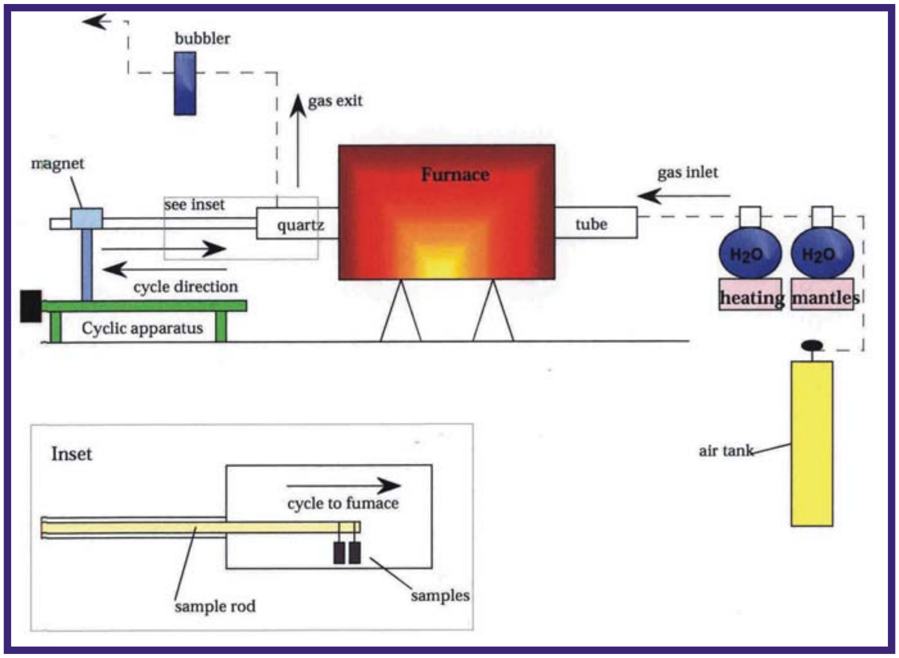

Figure 9: Schematic diagram of the apparatus used for cyclic oxidation exposures with controlled partial pressures of water vapor

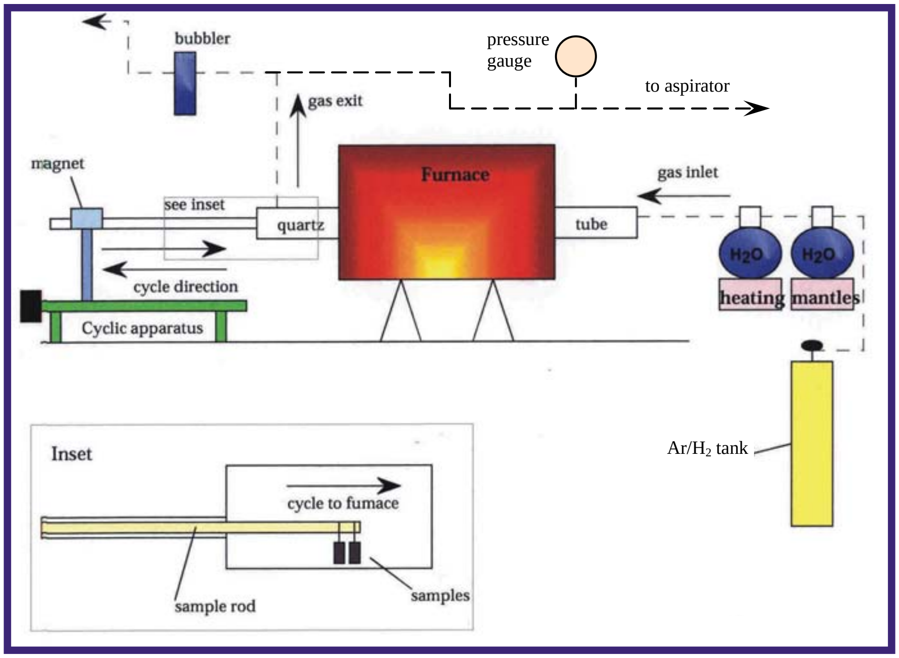

Figure 10: Schematic diagram of the apparatus used for cyclic oxidation exposures with Ar/H_2/H_2O

Two specimens of each alloy being studied were put into a furnace with one of the above atmospheres. The samples were periodically removed from the furnaces and weighed. Optical microscopy was performed to determine if there was any change in oxide appearance or if spallation had occurred. After approximately 1000 hours, one specimen of each alloy was removed from the furnace and mounted in cross-section. It was then examined on the SEM. The remaining samples were kept in the furnace for a total of 2000 hours. They also were removed from time to time, where they were weighed and examined with the optical microscope. After the 2000 hours were complete, the samples were removed, mounted, and examined on the SEM. The changes in mass were determined for each specimen and were plotted against the number of cycles.

2.2 SIGMA PHASE EXPERIMENTS

X-ray Diffraction (XRD) analysis was performed on a sample of 26 Cr Ferritic that had been exposed for 2000 hours in air + 0.1 atm H_2O at 700^oC. This was done to be certain that the sigma phase and not another phase was present in the 26 Cr Ferritic samples exposed in the atmospheres studied at 700^oC.

The composition of the sigma phase in the alloys in which it was seen (26 Cr Ferritic, 700^oC, the three atmospheres studied) was found using EDX on the SEM. The sigma phase compositions were then compared to the composition of the ferrite in the affected zone.

Samples of E-brite and 26 Cr Ferritic were exposed in dry air at 700^oC. After 50 hours, they were removed from the furnace and examined on the SEM. After SEM analysis, the specimens were returned to the furnace and removed every 50 hours, where the SEM was again used to establish when the sigma phase developed in these alloys. The experiments were performed for 500 hours to determine the amount of sigma phase that formed.

2.3 CONDUCTIVITY

The ASR of the oxide scales formed was measured at NETL in Morgantown, West Virginia. To make the electrodes for conductivity measurements, about half a micron of platinum was sputtered onto the surfaces of the alloy. Platinum paste was used to hold down a small piece of platinum mesh, onto which silver wires were welded (see Figure 11). Conductivity measurements were made at 900^oC and when the voltage drop stabilized, the temperature was dropped in 50°C increments to 700°C. The voltage drop across the samples was recorded for each temperature. The current was constant at 10mA.

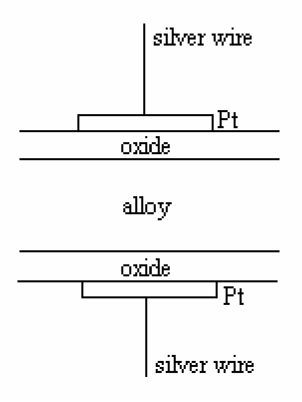

Figure 11: A schematic of the setup for the conductivity experiments

2.4 STRESS MEASUREMENTS

Two samples of Crofer were cyclically oxidized at 900°C for 100 hours, one in dry air and the other in air + 0.1 atm H_2O. XRD was performed on the samples in order to measure the stresses in the oxide. The strain in an oxide scale is determined by measuring the d-spacing of specific lattice planes, from which stress measurements can be made. The strain is given by:

$$\varepsilon_{\phi\psi} = \frac{d_{\phi\psi} - d_o}{d_o},$$

where $d_{\phi\psi}$ is the lattice spacing of the selected (hkl) planes for a given tilt ψ and d_o is the lattice spacing of these (hkl) planes for the stress-free case. The strain from the above equation is proportional to $\sin^2\psi$:

$$\frac{d_{\phi\psi} - d_o}{d_o} = \frac{1+\nu}{E}\sigma_\phi \sin^2\psi - \frac{\nu}{E}\left(\sigma_1 + \sigma_2\right).$$

The strain ($\varepsilon_{\phi\psi}$) can be plotted versus $\sin^2\psi$, and if the curve is linear, the slope of the line and values of the Young's Modulus (E), Poisson's ratio (ν), and d_o are used to calculate the stress.

Figure 12 shows the setup of the tilting technique[25], in which the intersection of the diffraction plane and the sample surface is the tilt axis. The diffraction plane contains the incident and diffracted x-ray beams, and it is fixed. When the normal to the sample surface is in the diffraction plane, the angle ψ is zero. As the sample is tilted and its surface normal is rotated out of the diffraction plane, ψ increases. Measurement of the stress involves only one set of (hkl) planes[30].

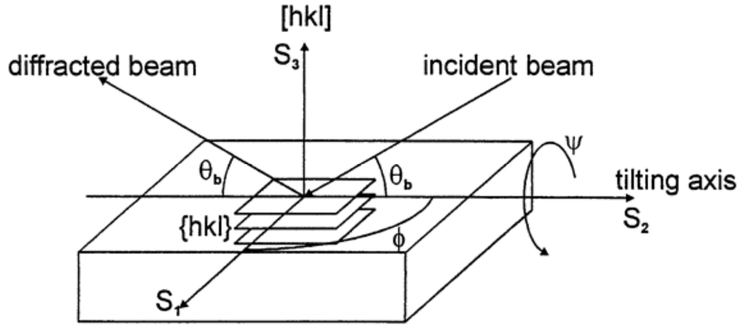

Figure 12: The setup for the tilting technique

3.0 RESULTS AND DISCUSSION

3.1 OXIDATION

3.1.1 700^oC, $Ar/H_2/H_2O$

Figure 13 shows the mass change vs. exposure time for samples at 700^oC in $Ar/H_2/H_2O$. The AL453 samples had the largest mass gains, followed by Crofer, 26 Cr Ferritic, and nickel.

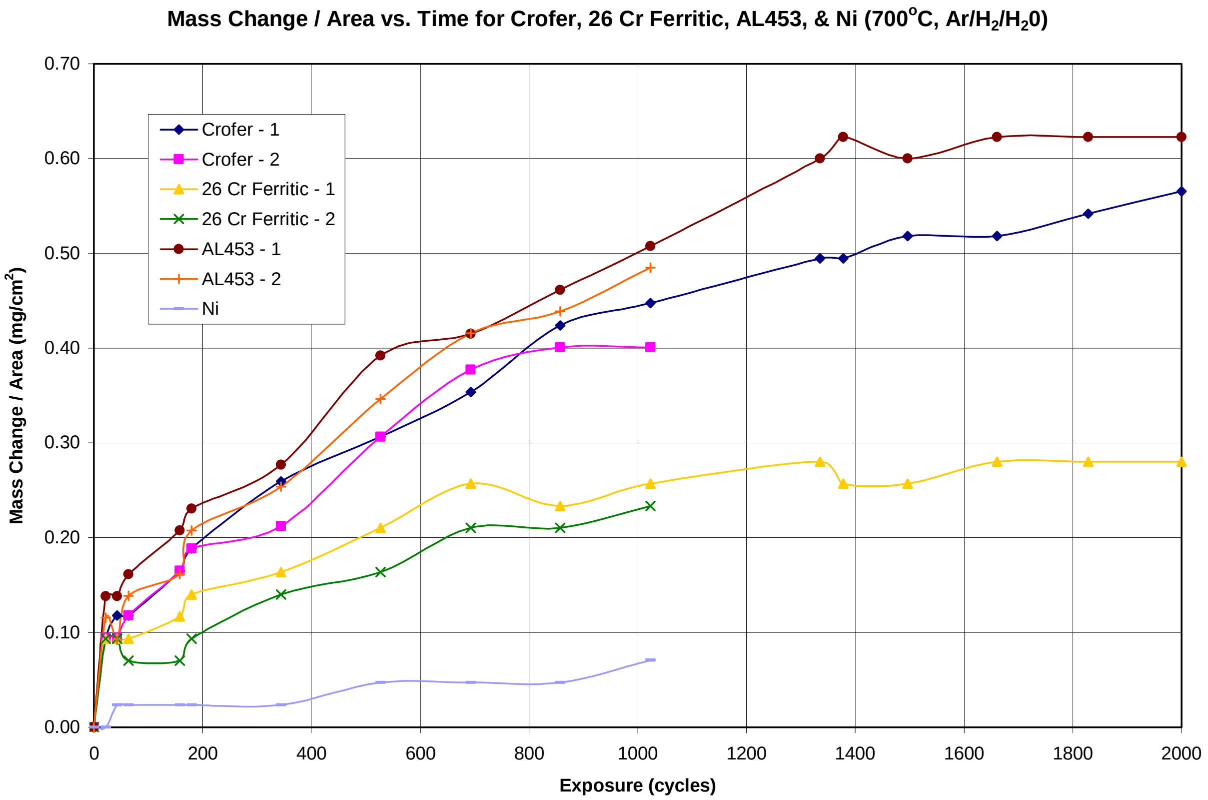

Figure 13: Mass Change vs. Exposure Time for Samples at 700°C in $Ar/H_2/H_2O$

Figure 14 shows the cross-sectional micrograph of Crofer after 2000 hours. A layer of manganese chromate was observed on the sample above the chromia scale. Internal oxidation of aluminum has occurred with this sample and can be seen below the oxide scale. There is also an area of silicon rich oxides just below the chromia layer. The cross-sectional micrograph for the 26 Cr Ferritic sample that had been exposed for 2000 hours is shown in Figure 15. Internal oxidation of aluminum can be seen beneath the oxide scale. Also, just below the chromia layer, there are some areas of oxides rich in silicon. The sigma phase can also be seen in the micrograph. Figure 16 shows the micrograph of the cross-section of AL453 after 2000 hours. A large amount of alumina has formed in this sample below the chromia scale. No micrographs were taken of nickel because the Ar-H_2 tank ran out of gas in the middle of the exposures and the nickel sample gained an unusually large amount of weight. Its exposure was stopped, and the last point recorded was the measurement taken just before the large weight gain.

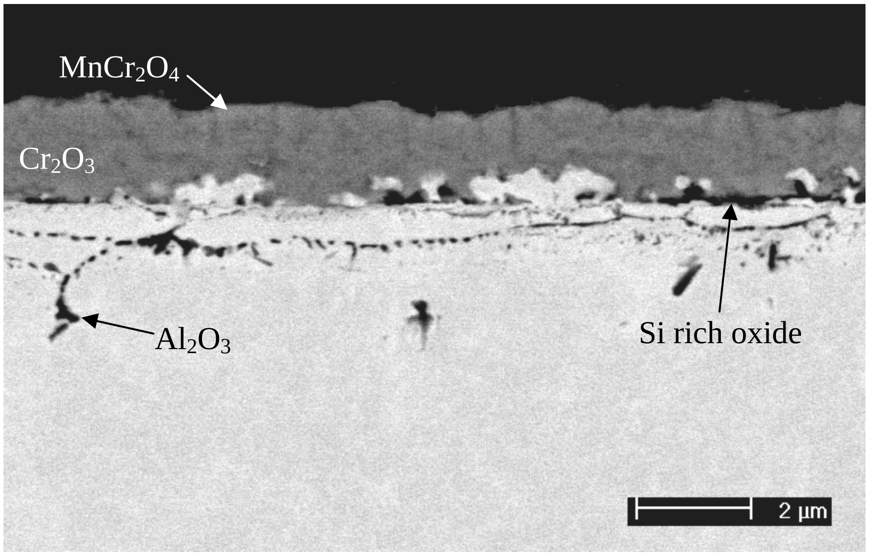

Figure 14: Crofer exposed at 700°C in Ar/H_2/H_2O for 2000 hours

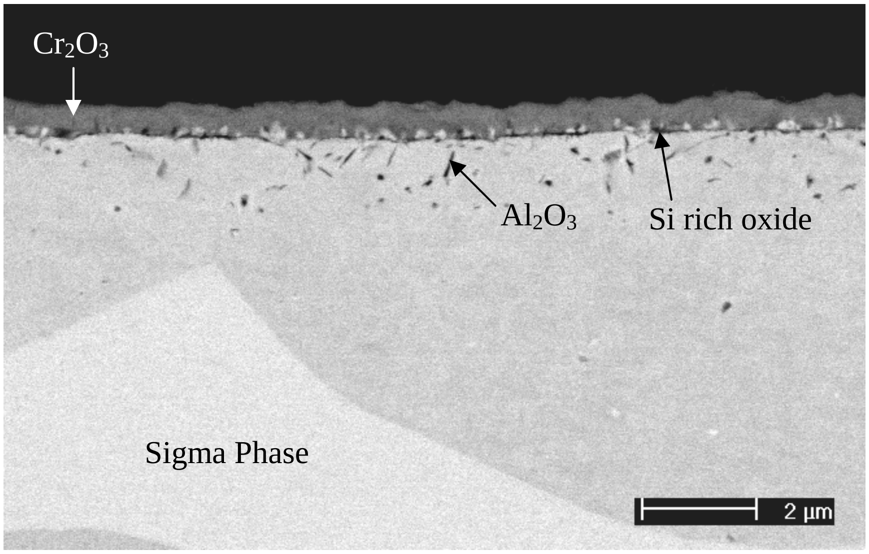

Figure 15: 26 Cr Ferritic exposed at 700°C in Ar/H_2/H_2O for 2000 hours

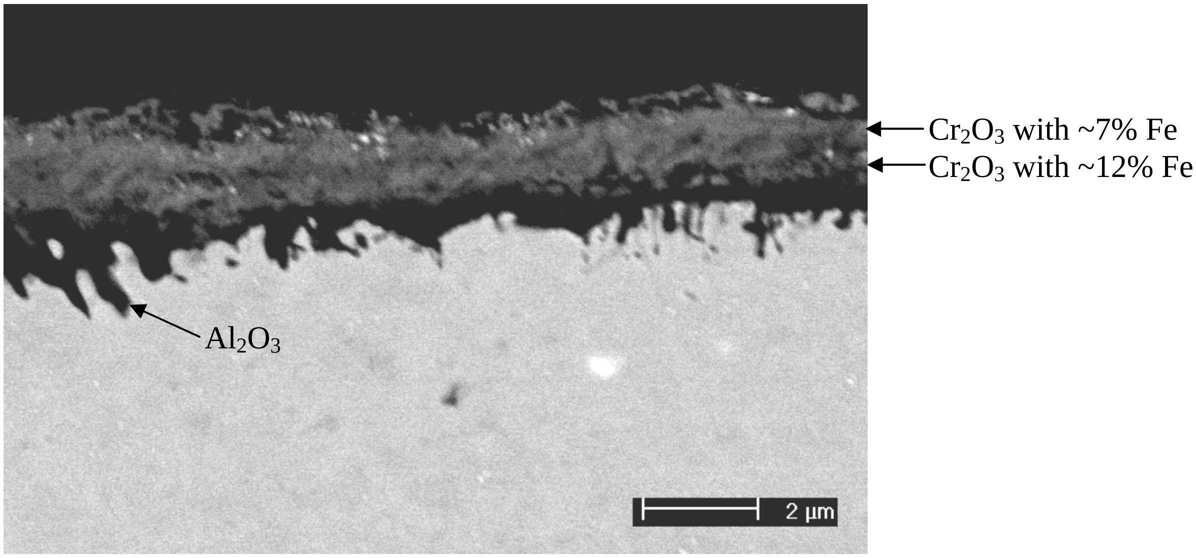

Figure 16: AL453 exposed at 700°C in Ar/H_2/H_2O for 2000 hours

3.1.2 700°C, Dry Air

Figure 17 shows the mass change vs. exposure time for samples at 700°C in dry air. The ZMG232 samples had the largest mass gains, followed by AL453, Crofer, 26 Cr Ferritic, and Modified AL453.

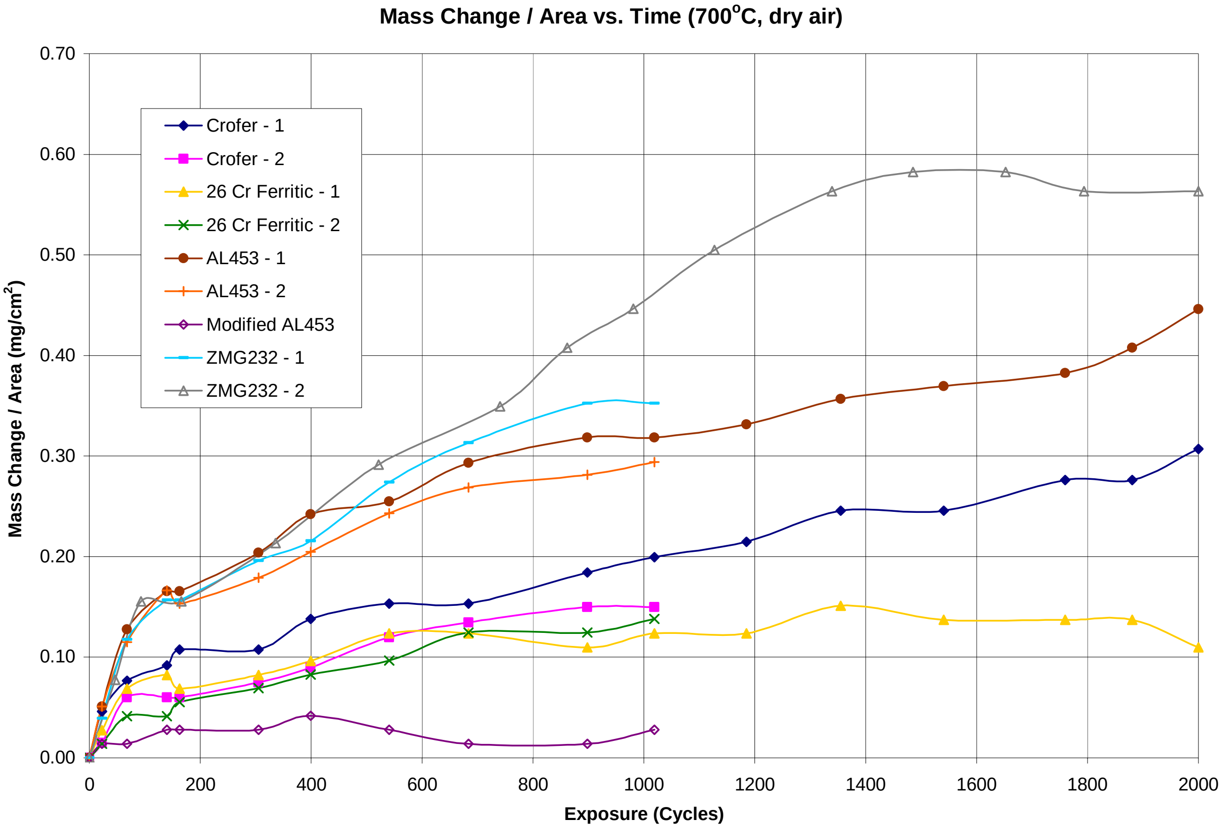

Figure 17: Mass Change vs. Exposure Time for Samples at 700°C in Dry Air

The cross-sectional micrograph of Crofer after 2000 hours is shown in Figure 18. Internal oxidation of aluminum has occurred with this sample and can be seen below the oxide scale, and a layer of manganese chromate was observed on the sample above the chromia scale. There are areas of oxides rich in silicon below the oxide layer. Figure 19 shows the micrograph for 26 Cr Ferritic after 2000 hours. Below the chromia scale, internal alumina can be seen. The sigma phase can also be seen in the micrograph. Also, directly below the oxide layer, areas of silicon rich oxides can be seen. The micrograph of the cross-section of AL453 after 2000 hours is shown in Figure 20. Again, there is internal oxidation of aluminum that has occurred below the oxide scale. A layer of iron-chromium has also occurred between the chromia scale and the internal oxidation zone. Figure 21 is the micrograph for Modified AL453 after 1019 hours. A chromia scale has formed on the surface of the sample, and directly below this, internal oxidation of aluminum has occurred and produced a continuous layer of alumina. The cross-sectional micrograph of ZMG232 after 2000 hours is shown in Figure 22. A layer of manganese chromate was observed on the sample above the chromia scale. Internal alumina can be seen below the oxide layer. Also, some areas of silicon rich oxide can be seen just beneath the chromia layer.

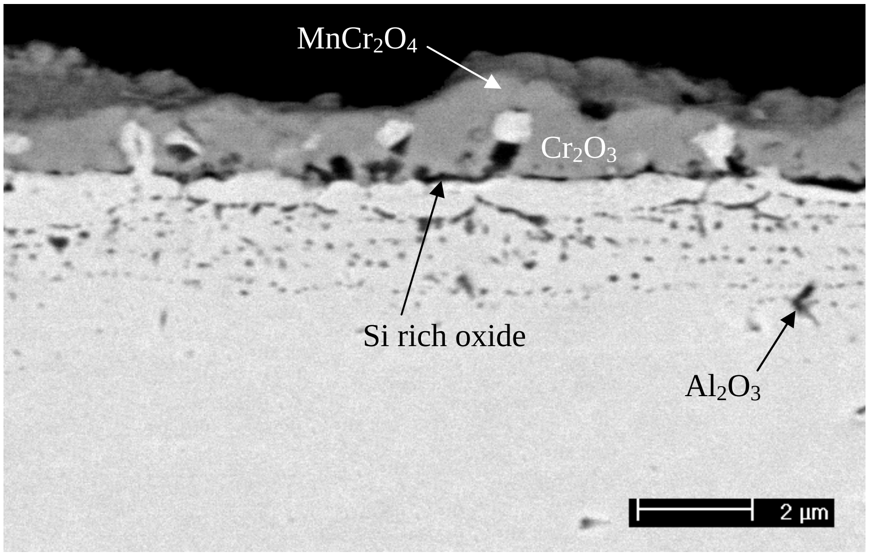

Figure 18: Crofer exposed at 700°C in Dry Air for 2000 hours

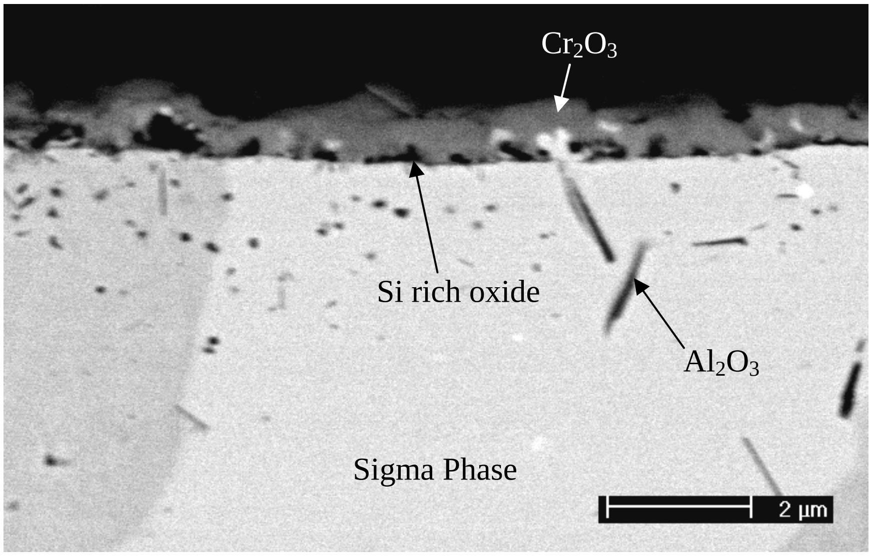

Figure 19: 26 Cr Ferritic exposed at 700°C in Dry Air for 2000 hours

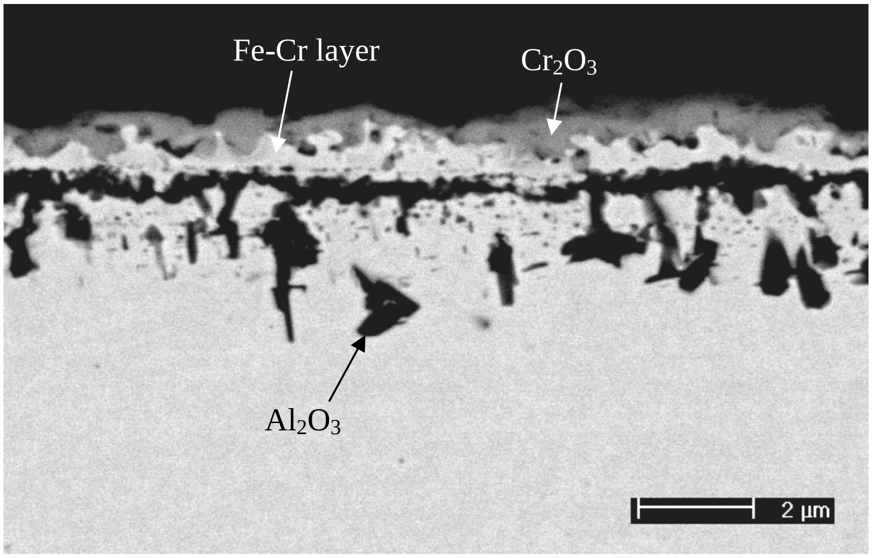

Figure 20: AL453 exposed at 700°C in Dry Air for 2000 hours

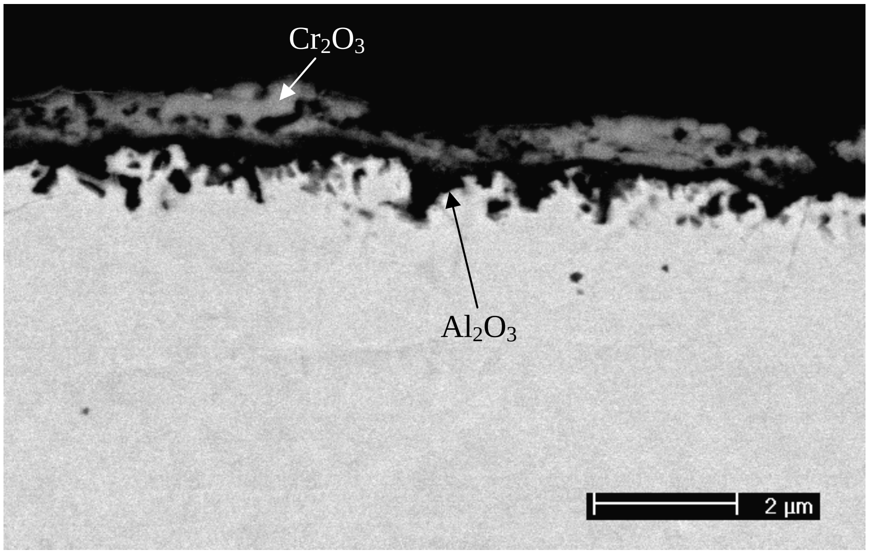

Figure 21: Modified AL453 exposed at 700°C in Dry Air for 1019 hours

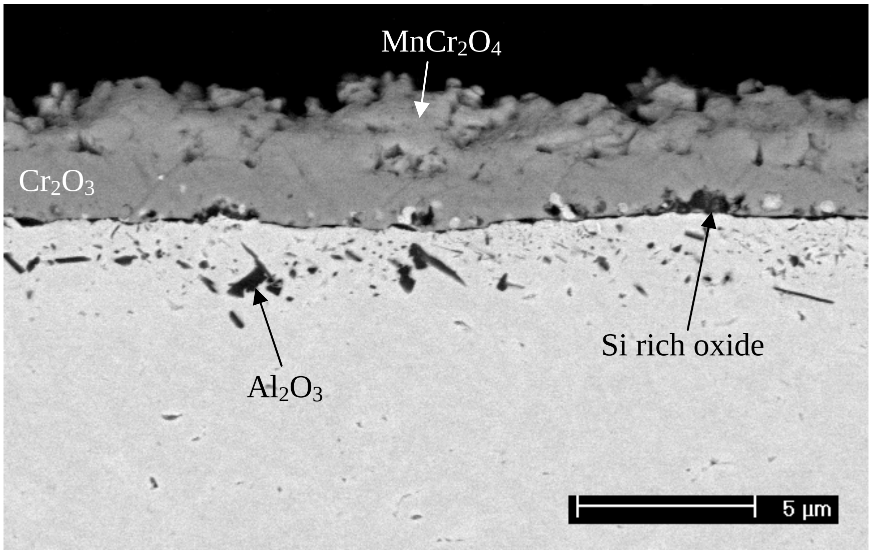

Figure 22: ZMG232 exposed at 700^oC in Dry Air for 2000 hours

3.1.3 700^oC, Air + 0.1 atm H_2O

Figure 23 shows the mass change vs. exposure time for Crofer, 26 Cr Ferritic, AL453, and ZMG232 at 700^oC in air + 0.1 atm H_2O, and the mass change vs. exposure time for nickel at 700^oC in Air + 0.1 atm H_2O is shown in Figure 24. Nickel had the largest mass gains, followed by AL453, Crofer, ZMG232, Modified AL453, and 26 Cr Ferritic.

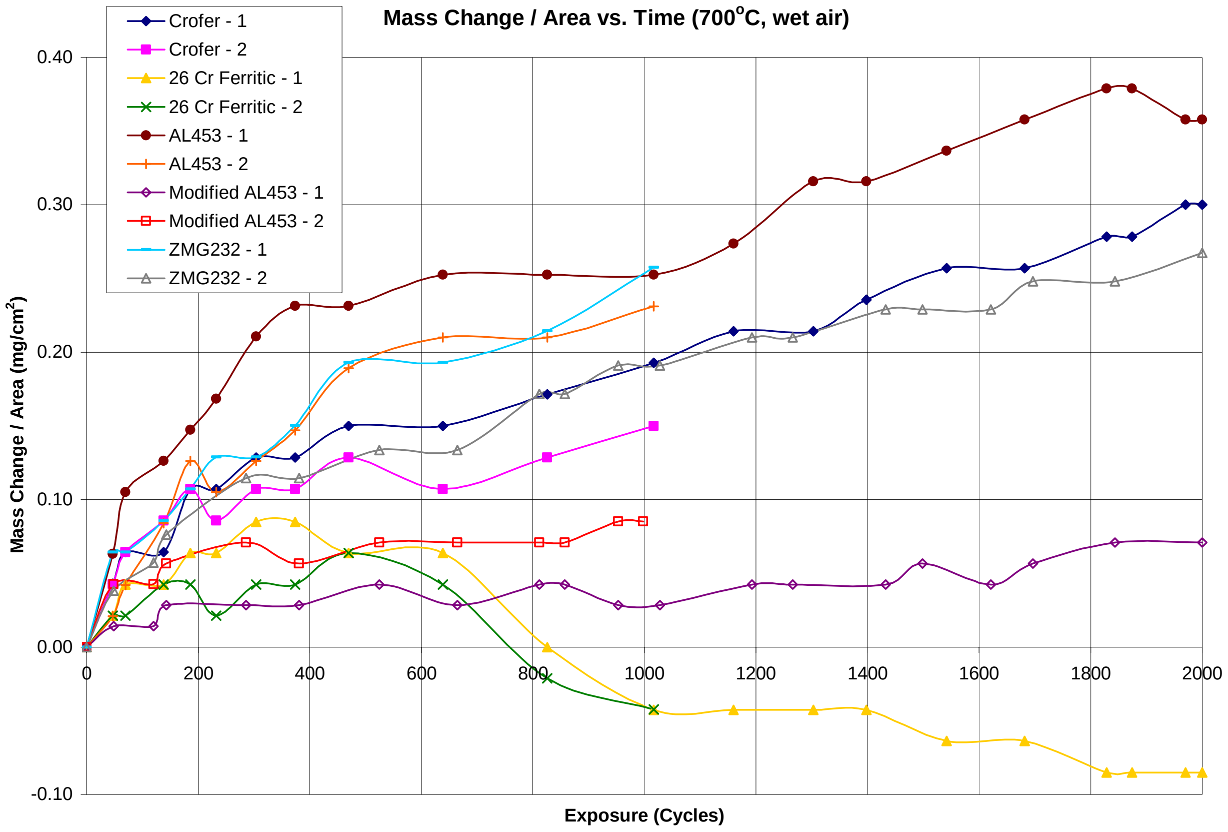

Figure 23: Mass Change vs. Exposure Time for Crofer, 26 Cr Ferritic, AL453, Modified AL453, and ZMG232 at 700°C in Air + 0.1 atm H_2O

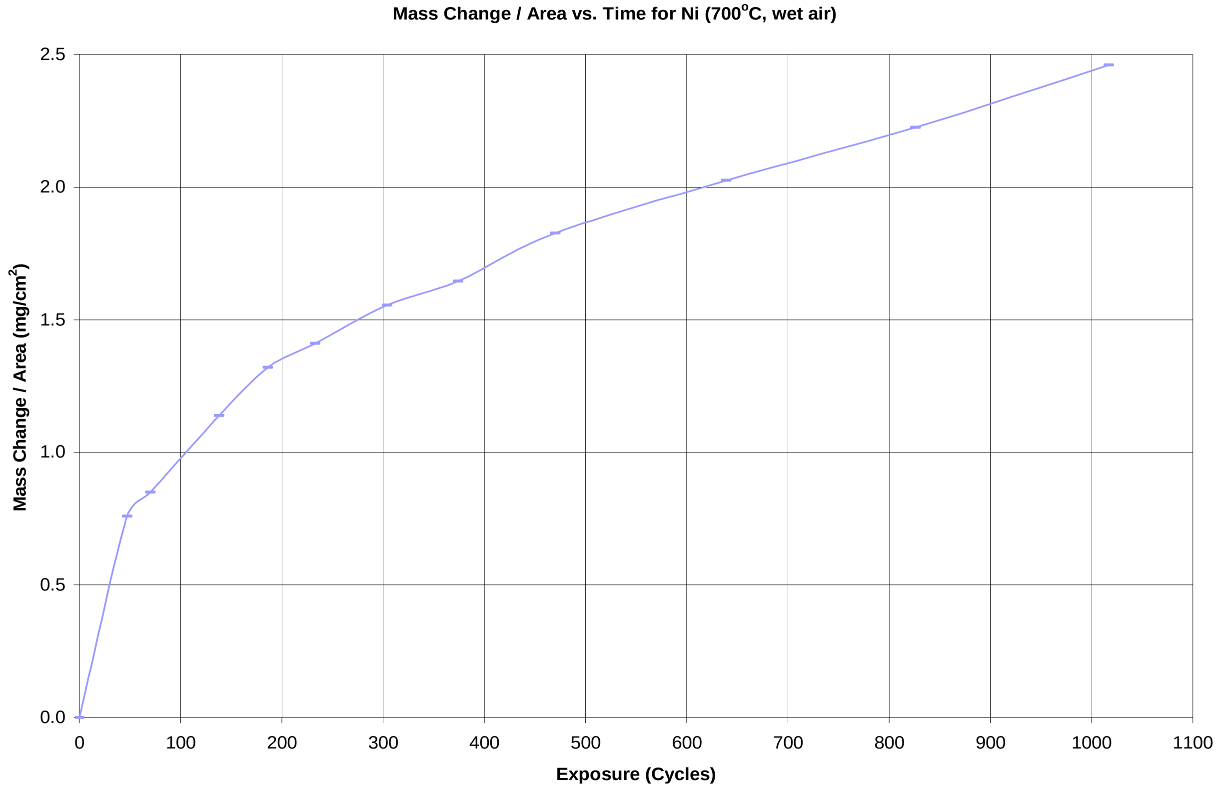

Figure 24: Mass Change vs. Exposure Time for Nickel at 700°C in Air + 0.1 atm H_2O

Figure 25 shows the cross-sectional micrograph of Crofer after 2000 hours. A layer of manganese chromate was observed on the sample above the chromia scale. Also, internal oxidation of aluminum has occurred with this sample and can be seen below the oxide scale. There are also areas of silicon rich oxide that can be seen beneath the surface. The micrograph for 26 Cr Ferritic after 2000 hours is shown in Figure 26. Internal alumina can be seen below the chromia scale, and the sigma phase can be seen as well. A layer of manganese chromate was observed on the surface in some areas. The micrograph of AL453 exposed for 2000 hours is shown in Figure 27. Again, there is internal oxidation of aluminum that has occurred below the oxide scale. A small layer of metallic iron-chromium has also formed between the chromia scale and the internal oxidation zone. Figures 28 and 29 show micrographs of Modified AL453 after 2000 hours of exposure. In Figure 28, a layer of iron-chromium that is rich in aluminum, silicon, and oxygen is seen above the alloy. A chromia layer rich in Al and Si was seen on the surface of the alloy in Figure 29. Just beneath the oxide is a continuous layer of internal alumina. The aluminum, silicon, and oxygen rich iron-chromium layer can also be seen in the micrograph. The cross-sectional micrograph of ZMG232 after 2000 hours is shown in Figure 30. A manganese chromate layer was observed on the sample above the chromia scale. Internal alumina can be seen below the oxide layer. Figure 31 shows the micrograph for nickel after 1017 hours. A layer of nickel oxide was seen on the surface of the sample. There was much porosity in the oxide layer, and an interface is observed between the nickel oxide scales that are grown by outward nickel migration and inward oxygen migration.

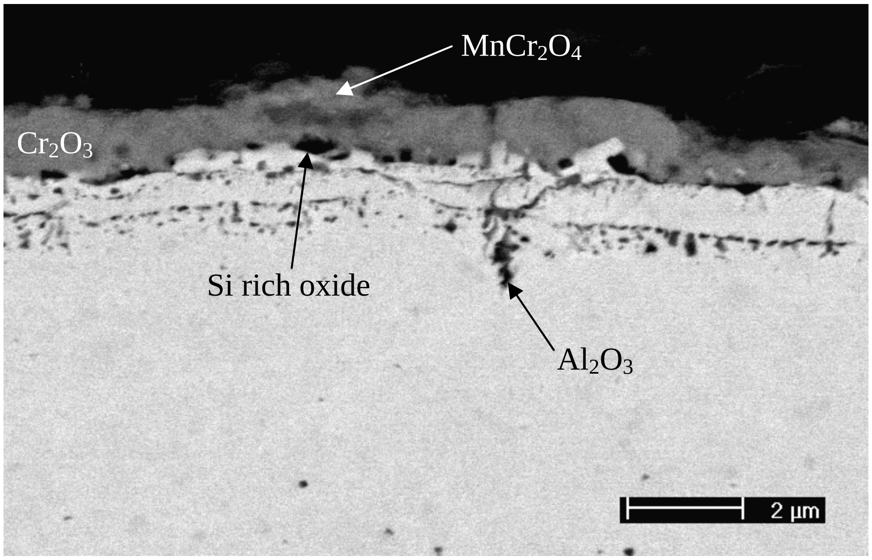

Figure 25: Crofer exposed at 700°C in Air + 0.1 atm H_2O for 2000 hours

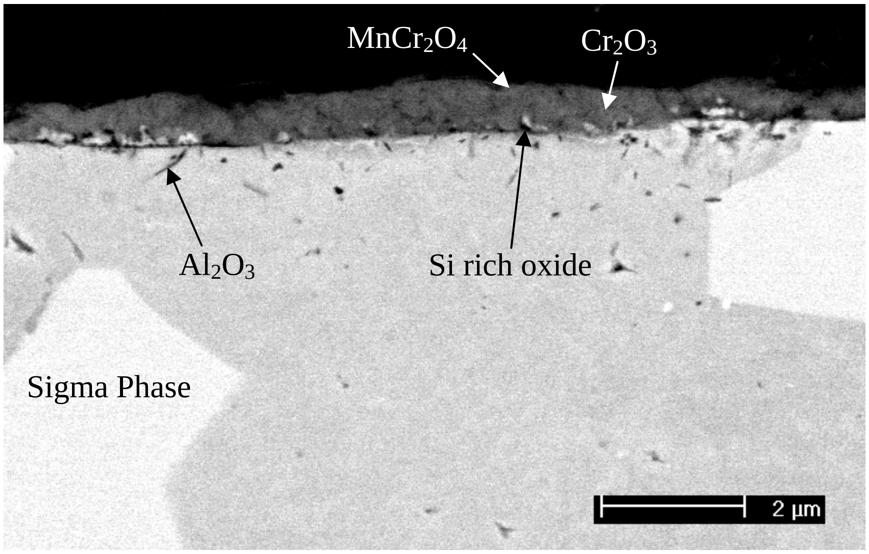

Figure 26: 26 Cr Ferritic exposed at 700°C in Air + 0.1 atm H_2O for 2000 hours

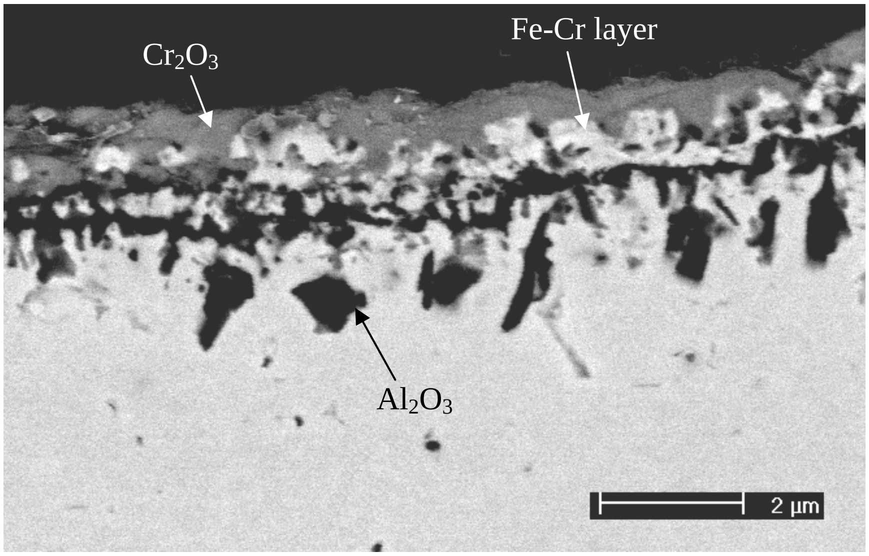

Figure 27: AL453 exposed at 700°C in Air + 0.1 atm H_2O for 2000 hours

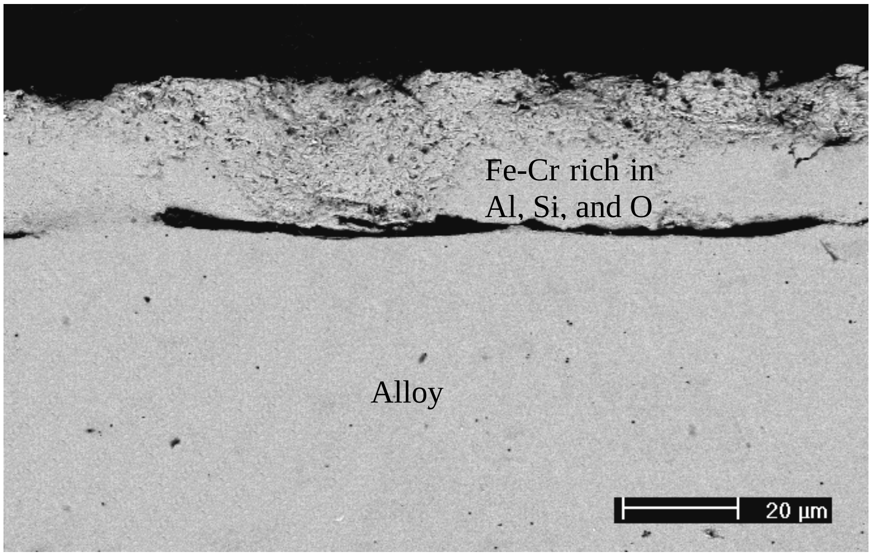

Figure 28: Modified AL453 exposed at 700^oC in Air + 0.1 atm H_2O for 2000 hours

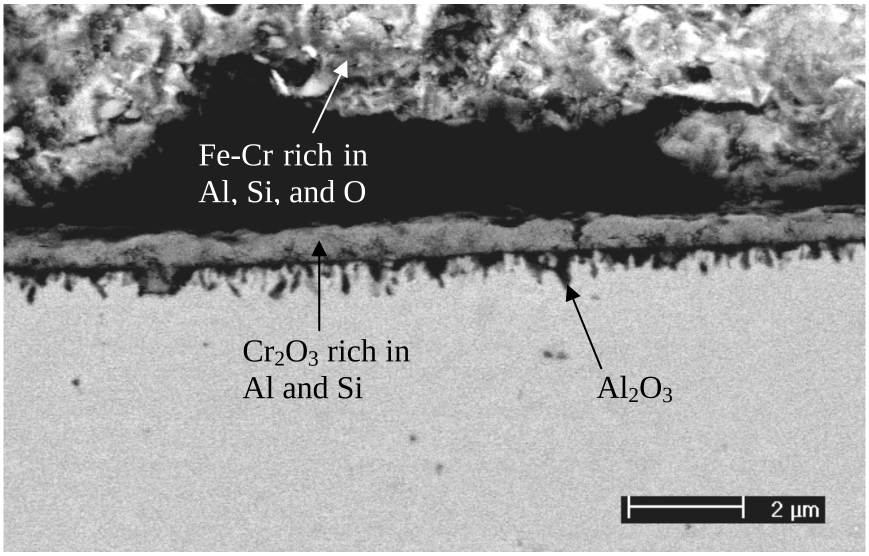

Figure 29: Modified AL453 exposed at 700^oC in Air + 0.1 atm H_2O for 2000 hours

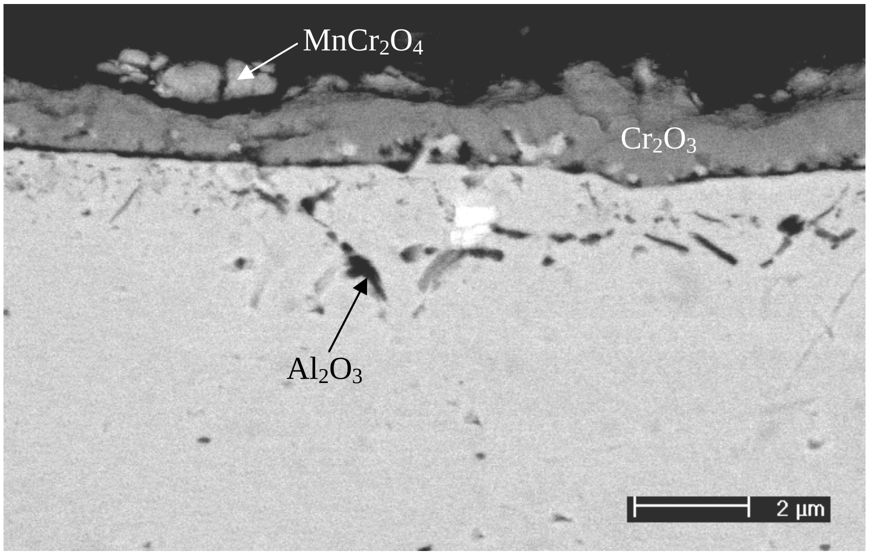

Figure 30: ZMG232 exposed at 700°C in Air + 0.1 atm H_2O for 2000 hours

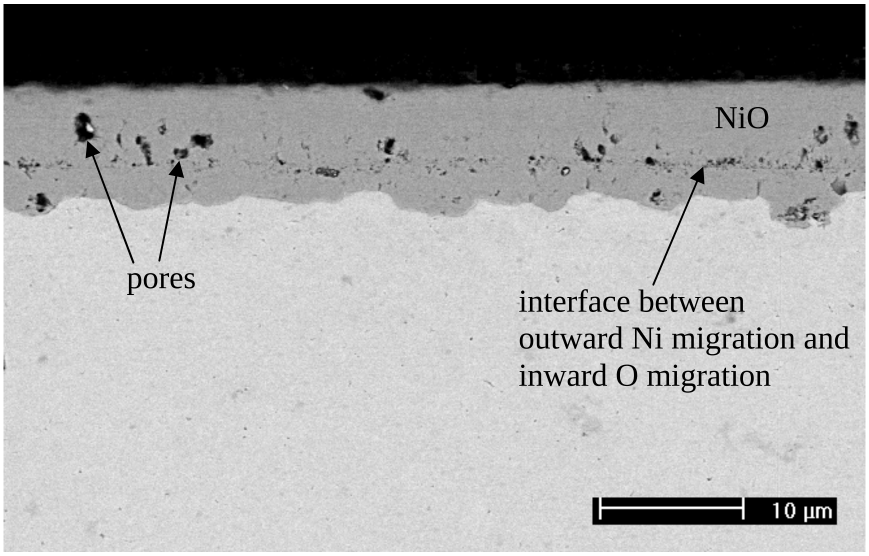

Figure 31: Nickel exposed at 700°C in Air + 0.1 atm H_2O for 1017 hours

3.1.4 800^{o}C, Air + 0.1 atm H_2O

The mass change vs. exposure time for JS-3, Crofer, New Crofer, E-brite, and 26 Cr Ferritic in air + 0.1atm H_2O at 800^{o}C is shown in Figure 32, and Figure 33 shows the mass change vs. exposure time for Type 304 stainless steel at 800^{o}C in air + 0.1atm H_2O. Crofer had the largest mass gains, followed by New Crofer, JS-3, E-brite, 26 Cr Ferritic, and Type 304 stainless steel.

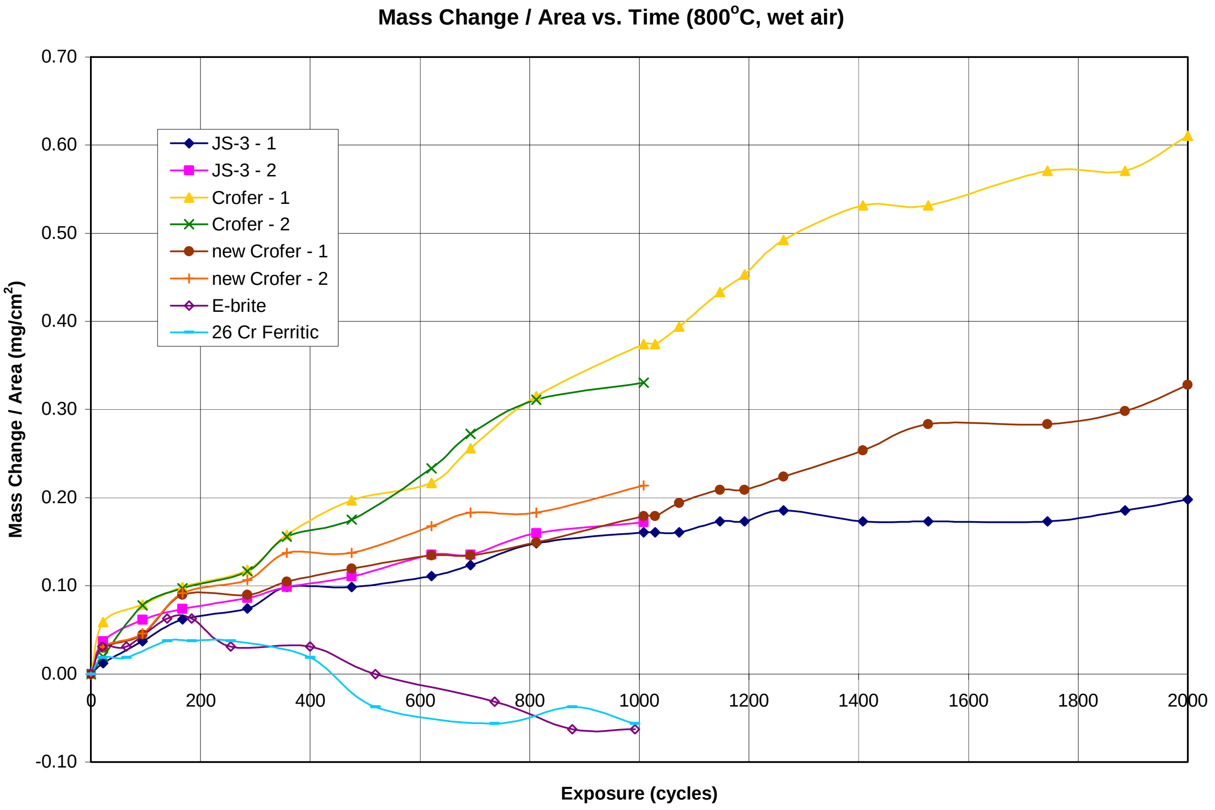

Figure 32: Mass Change vs. Exposure Time for JS-3, Crofer, New Crofer, E-brite, and 26 Cr Ferritic at 800^{o}C in Air + 0.1 atm H_2O

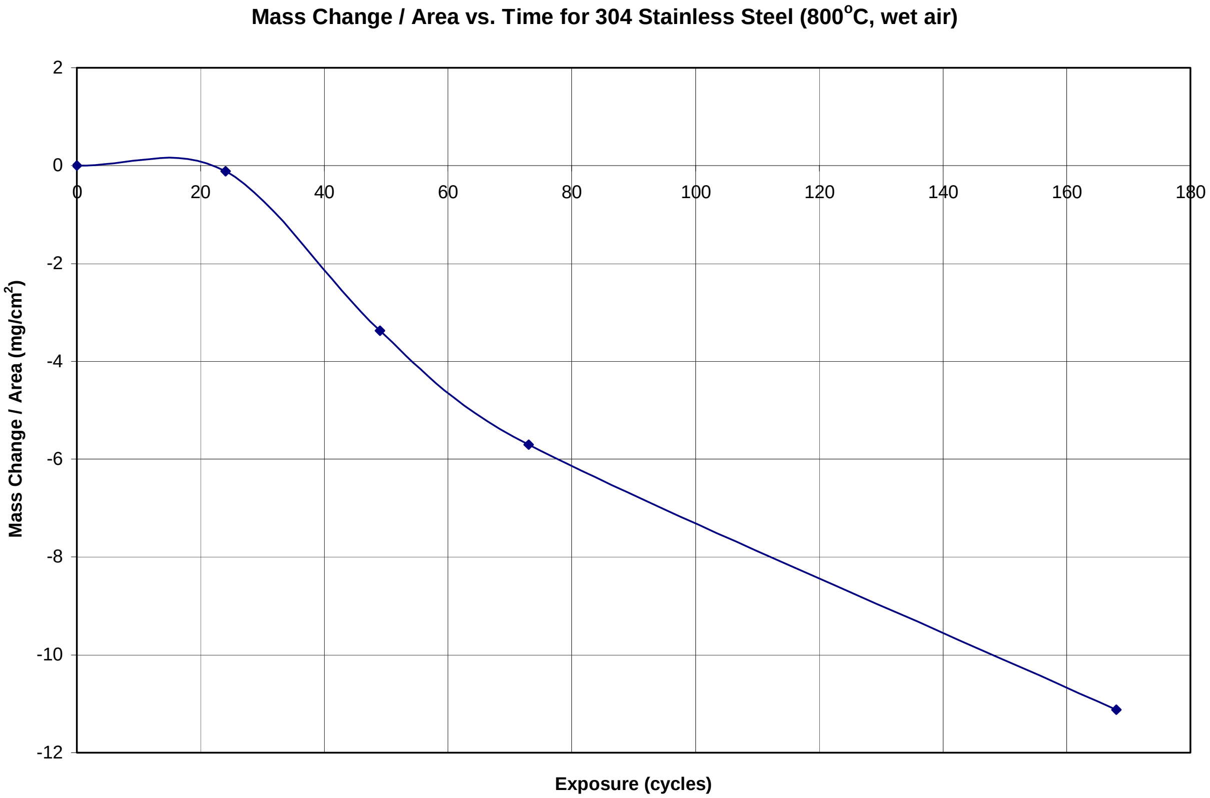

Figure 33: Mass Change vs. Exposure Time for Type 304 Stainless Steel at 800°C in Air + 0.1 atm H_2O

The cross-sectional micrograph of JS-3 after 2000 hours is shown in Figure 34. In most places, a thin layer of manganese chromate was observed above the chromia layer. Internal oxidation of aluminum has also occurred, and the alumina particles can be seen below the surface. There are also a few areas of silicon rich oxides just below the oxide layer. Figure 35 shows the micrograph of Crofer that had been exposed for 2000 hours. A thin layer of manganese chromate has formed above the layer of chromia. Again, there is internal oxidation of aluminum which can be seen below the oxide layer. Also, just beneath the chromia layer, silicon rich oxides were observed. The micrograph for New Crofer after 2000 hours is shown in Figure 36. Internal oxidation of aluminum has occurred with this sample and can be observed beneath the surface. There were also a few small areas of silicon rich oxide below the chromia. Additionally, a thin layer of manganese chromate was found above the chromia layer. Figure 37 shows the micrograph of E-brite after 992 hours. A thin layer of chromia was observed on the surface of this sample. Again, aluminum had internally oxidized and could be found below the chromia layer. There were also silicon rich oxides just beneath the oxide layer. Figure 38 shows the micrograph of 26 Cr Ferritic that had been exposed for 992 hours. There are a few areas of manganese chromate that have formed above the chromia layer. Just beneath the oxide scale, a few regions of silicon rich oxide were observed. Internal oxidation of aluminum has also occurred. The micrograph of Type 304 stainless steel after 168 hours is shown in Figure 39. Chromia rich in manganese and iron was found on the surface. Above the chromia layer, an oxide rich in nickel, chromium, and iron was observed in some areas. Other areas above the chromia contained iron oxide rich in nickel, chromium, and manganese.

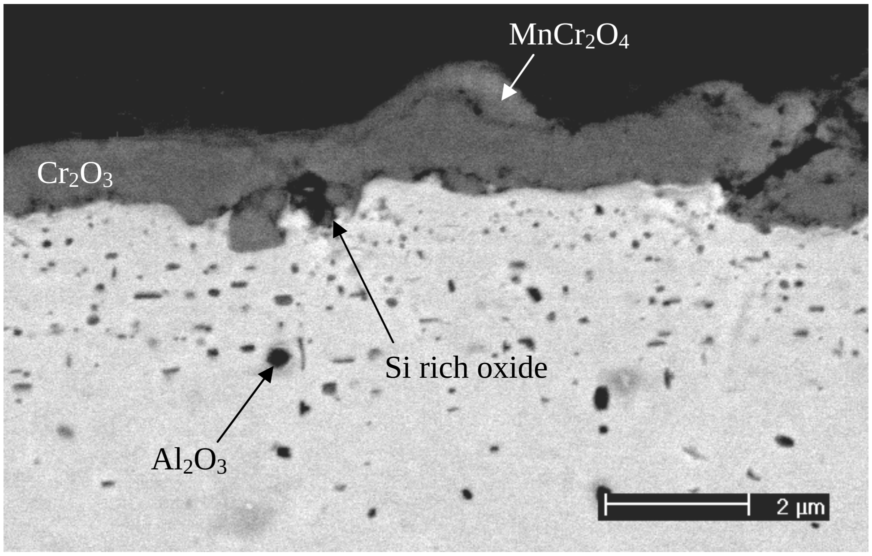

Figure 34: JS-3 exposed at 800°C in Air + 0.1 atm H_2O for 2000 hours

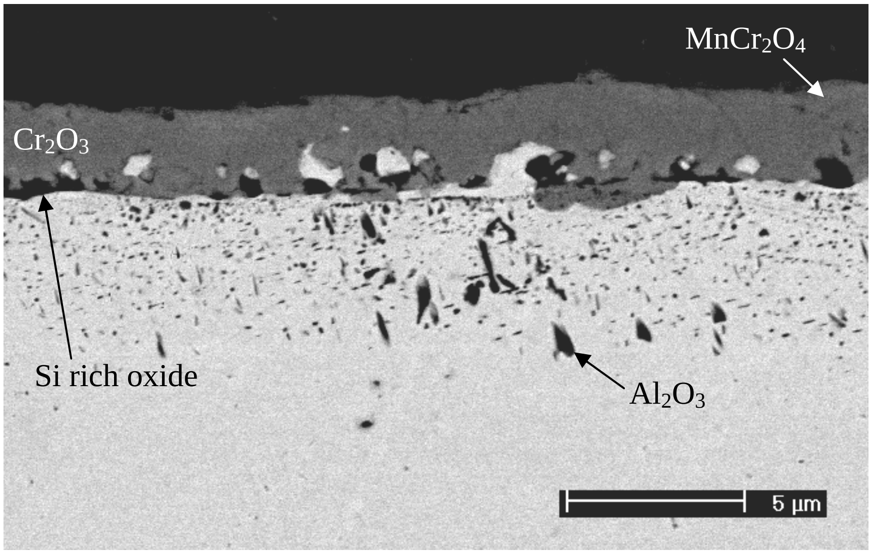

Figure 35: Crofer exposed at 800°C in Air + 0.1 atm H_2O for 2000 hours

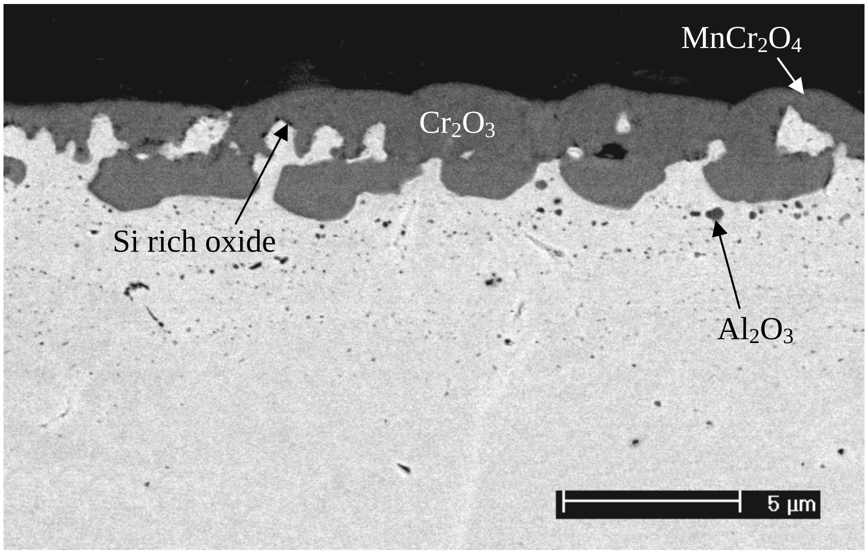

Figure 36: New Crofer exposed at 800°C in Air + 0.1 atm H_2O for 2000 hours

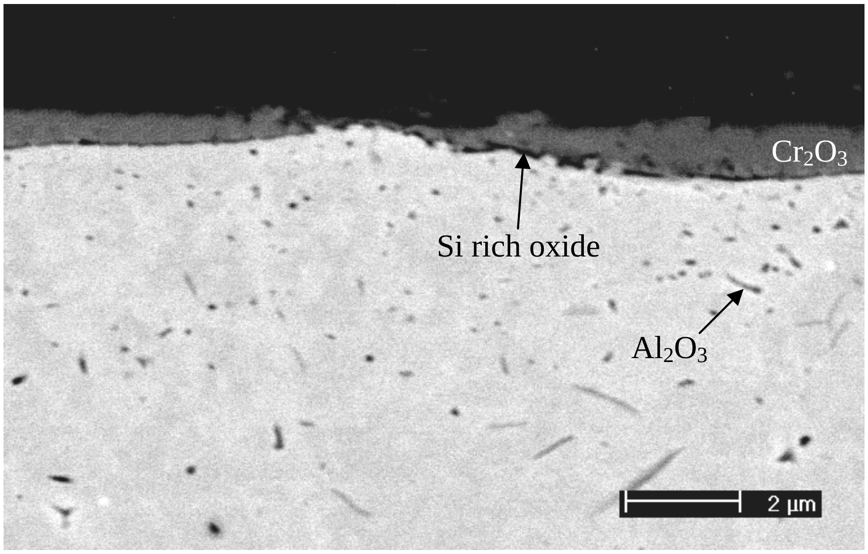

Figure 37: E-brite exposed at 800°C in Air + 0.1 atm H_2O for 992 hours

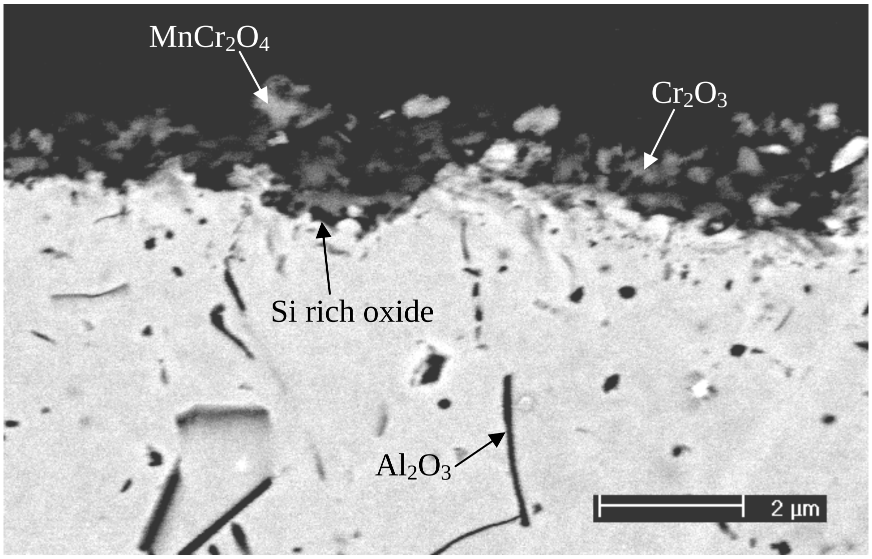

Figure 38: 26 Cr Ferritic exposed at 800°C in Air + 0.1 atm H_2O for 992 hours

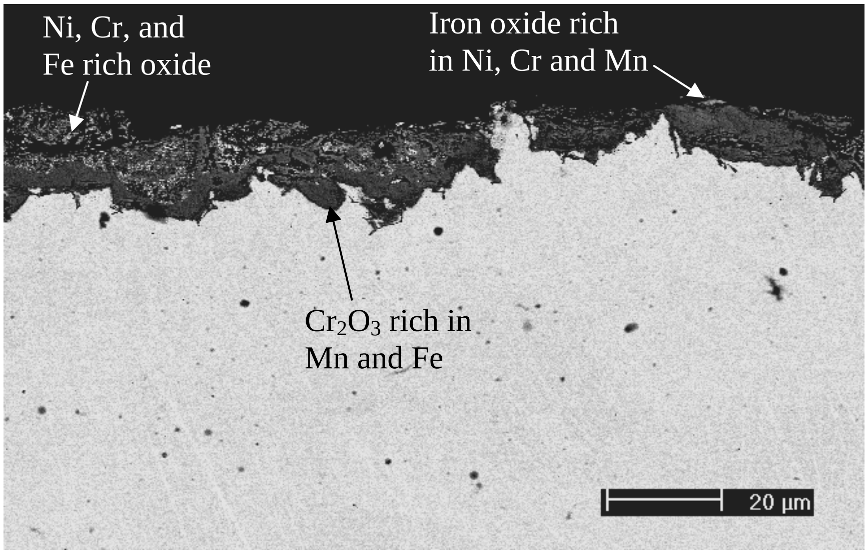

Figure 39: Type 304 Stainless Steel exposed at 800°C in Air + 0.1 atm H_2O for 168 hours

3.1.5 900^{o}C, Ar/H_2/H_2O

Figure 40 shows the mass change vs. exposure time for samples at 900^{o}C in Ar/H_2/H_2O. The AL453 samples had the largest mass gains, followed by 26 Cr Ferritic, and then Crofer.

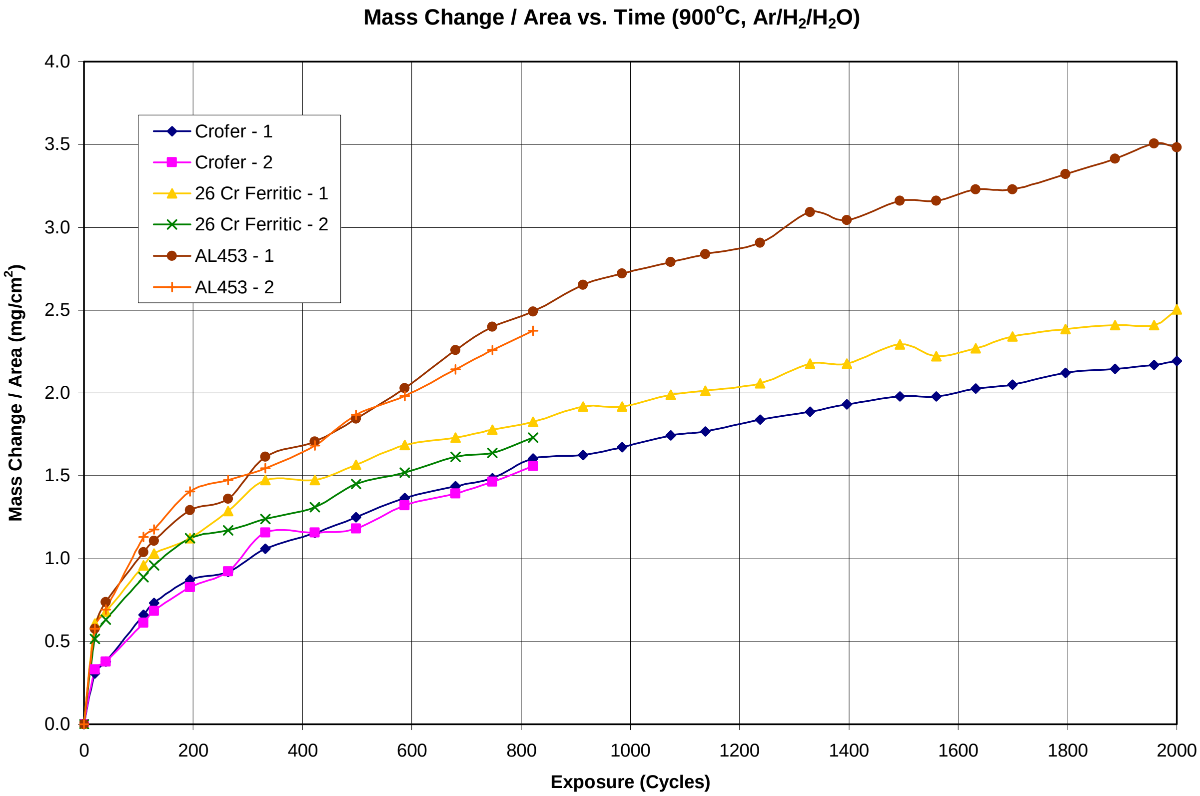

Figure 40: Mass Change vs. Exposure Time for Samples at 900^{o}C in Ar/H_2/H_2O

Figure 41 shows the cross-sectional micrograph of Crofer after 2000 hours. A layer of manganese chromate was observed on the sample above the chromia scale. Internal oxidation of aluminum has occurred with this sample and can be seen below the oxide scale. The cross-sectional micrograph for the 26 Cr Ferritic sample that had been exposed for 2000 hours is shown in Figure 42. A thin layer of manganese chromate was seen above the chromia scale. Alumina particles can be seen beneath the oxide scale. Also, just below the chromia layer, areas of oxides rich in silicon can be seen. Figure 43 shows the micrograph of the cross-section of AL453 after 2000 hours. A large amount of internal oxidation of aluminum has occurred in this sample. There is also an area of metallic iron-chromium between the chromia scale and the internal oxidation zone.

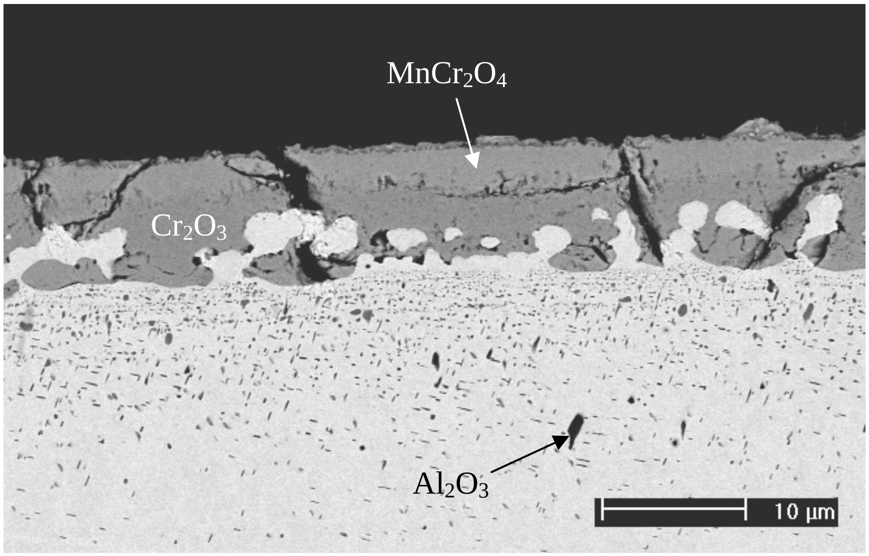

Figure 41: Crofer exposed at 900^{o}C in Ar/H_2/H_2O for 2000 hours

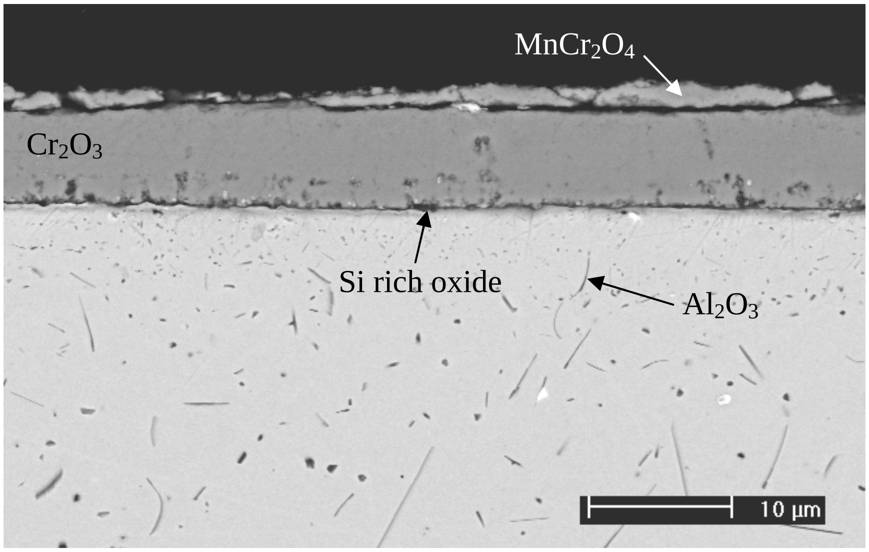

Figure 42: 26 Cr Ferritic exposed at 900^{o}C in Ar/H_2/H_2O for 2000 hours

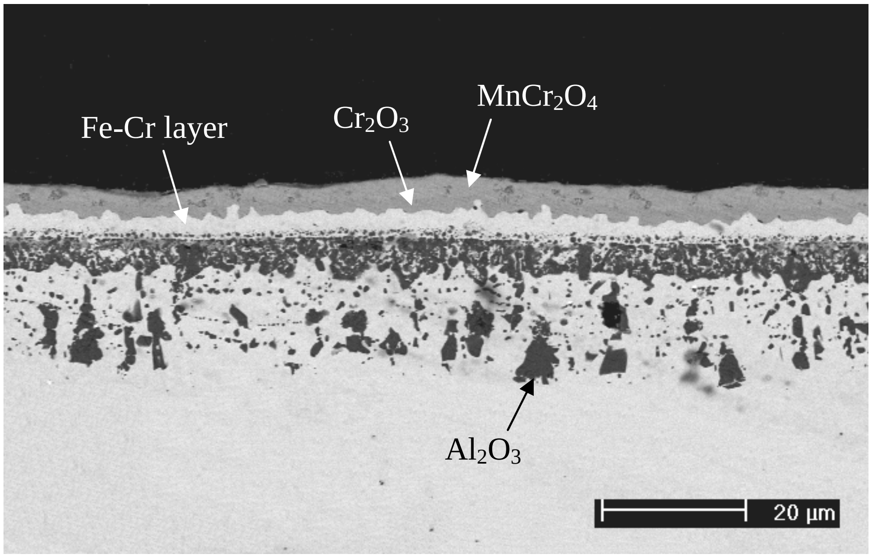

Figure 43: AL453 exposed at 900^{o}C in Ar/H_2/H_2O for 2000 hrs

3.1.6 900°C, Dry Air

Figure 44 shows the mass change vs. exposure time for samples at 900°C in dry air. The ZMG232 samples had the largest mass gains, followed by AL453, Crofer, and then 26 Cr Ferritic.

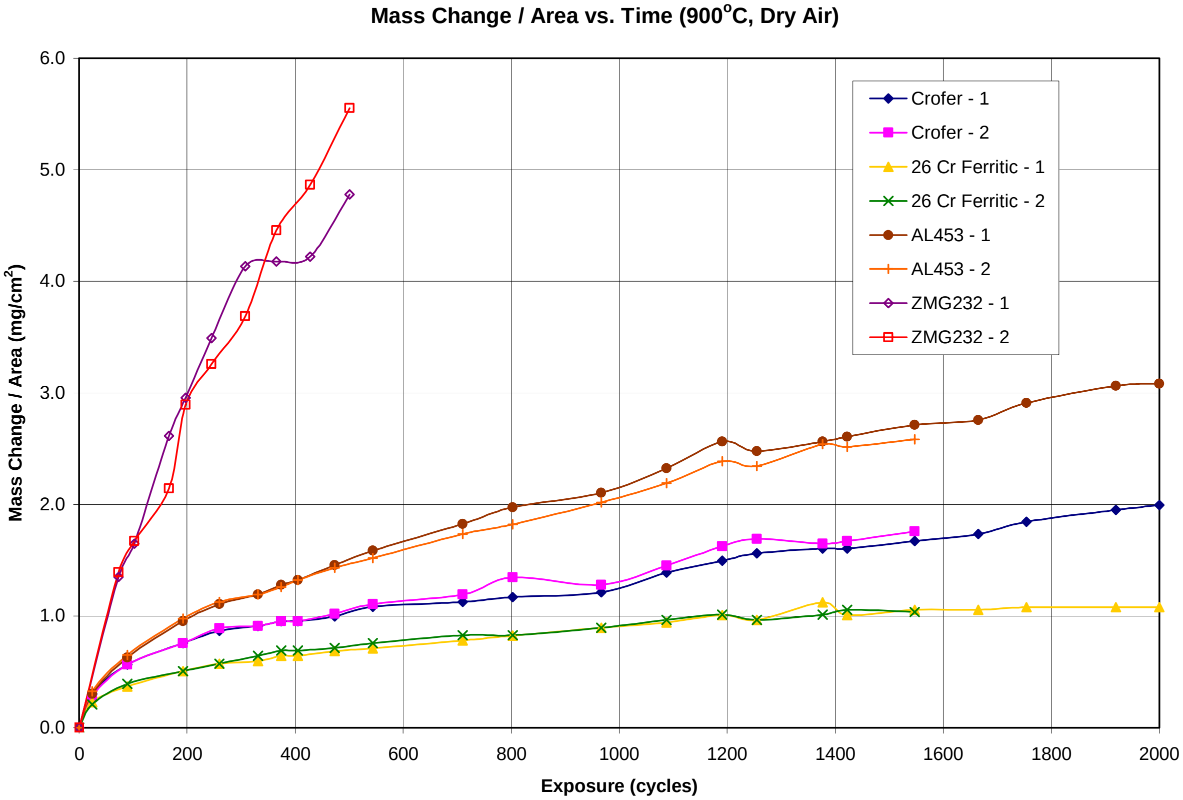

Figure 44: Mass Change vs. Exposure Time for Samples at 900°C in Dry Air (data for Crofer, 26 Cr Ferritic, and AL453 from Reference 31, data for ZMG232 from own research)

The cross-sectional micrograph of Crofer after 2000 hours is shown in Figure 45. A layer of manganese chromate was observed on the sample above the chromia scale. Internal oxidation of aluminum has occurred with this sample and can be seen below the oxide scale. Figure 46 is the cross-sectional micrograph for 26 Cr Ferritic after 2000 hours. Again, internal oxidation of aluminum has occurred and can be seen below the chromia layer. Also, just below the chromia scale is an area of silicon rich oxides. The AL453 micrograph for the sample exposed for 2000 hours is shown in Figure 47. Aluminum has internally oxidized and can be seen below the chromia layer. Also, there is a metal layer between the oxide layer and the internal oxidation. Figure 48 shows the micrograph of ZMG232 exposed for 501 hours. A layer of manganese chromate can be seen above the chromia layer. Also, just below the oxide scale, an area of silicon rich oxides has formed. Internal oxidation of aluminum has occurred, and can be observed below the surface.

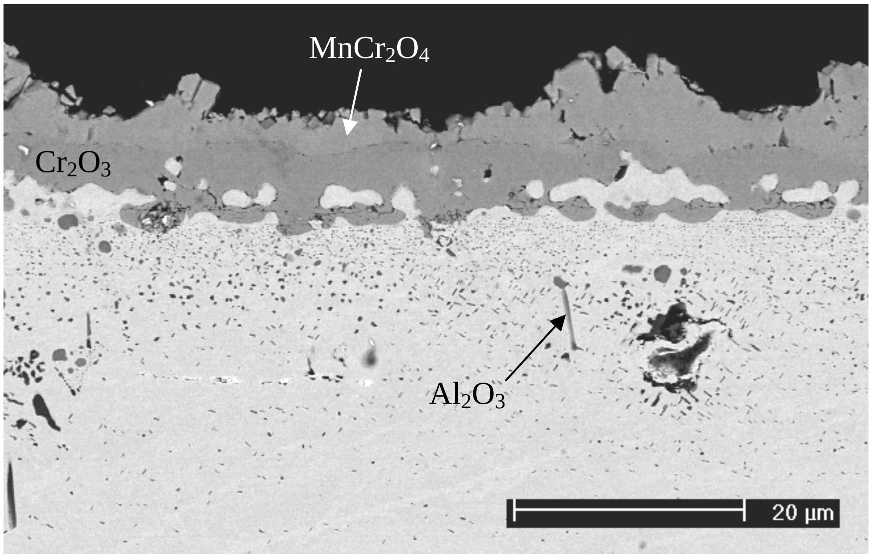

Figure 45: Crofer exposed at 900^{o}C in Dry Air for 2000 hours (from Reference 31)

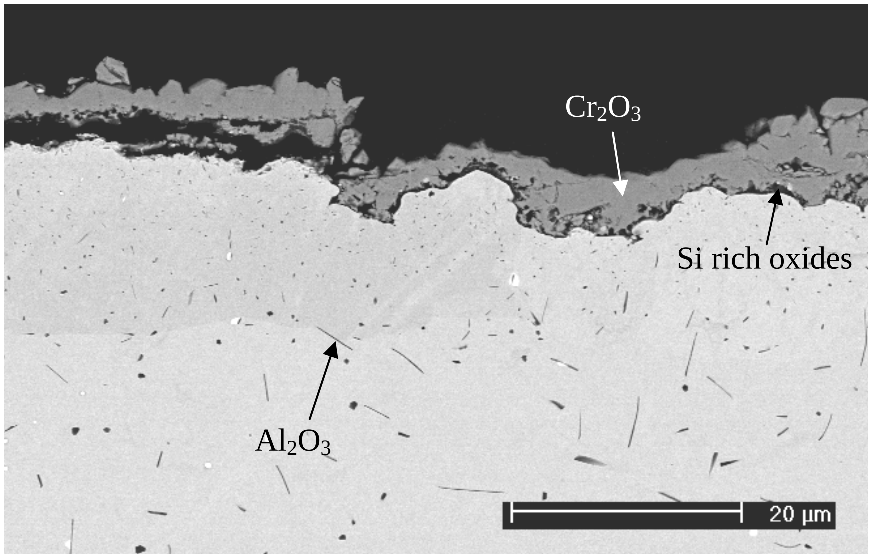

Figure 46: 26 Cr Ferritic exposed at 900°C in Dry Air for 2000 hours (from Reference 31)

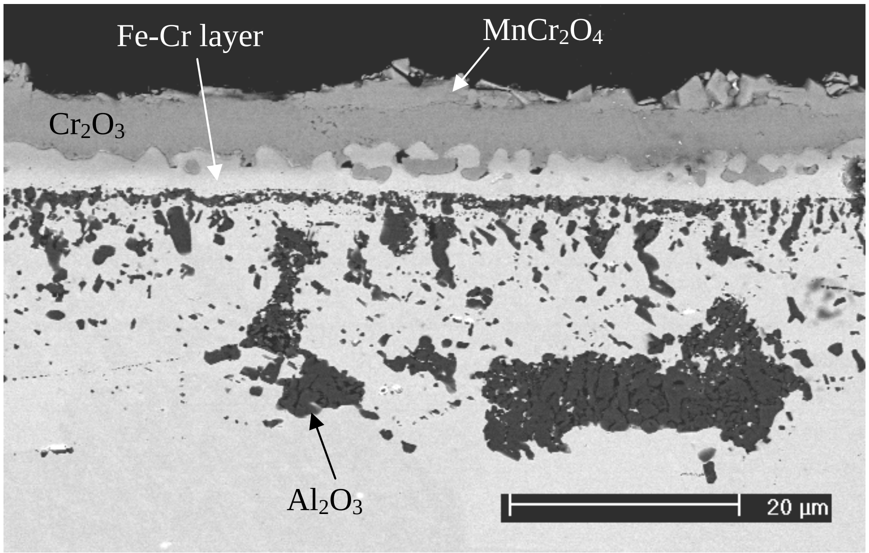

Figure 47: AL453 exposed at 900°C in Dry Air for 2000 hours (from Reference 31)

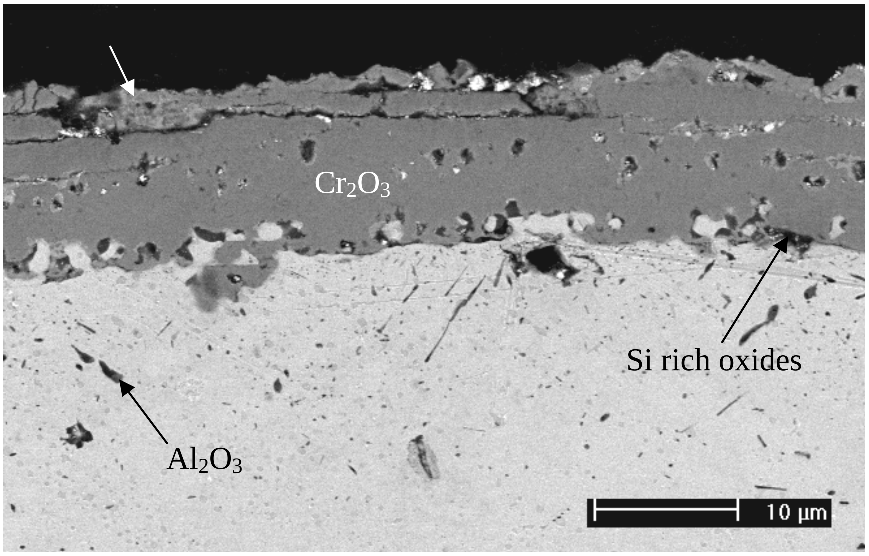

Figure 48: ZMG232 exposed at 900^{o}C in Dry Air for 501 hours

3.1.7 900^{o}C, Air + 0.1 atm H_2O

The mass change vs. exposure time for samples at 900^{o}C in Air + 0.1 atm H_2O is shown in Figure 49. The Crofer samples had the largest mass gains, followed by AL453, ZMG232, and then 26 Cr Ferritic.

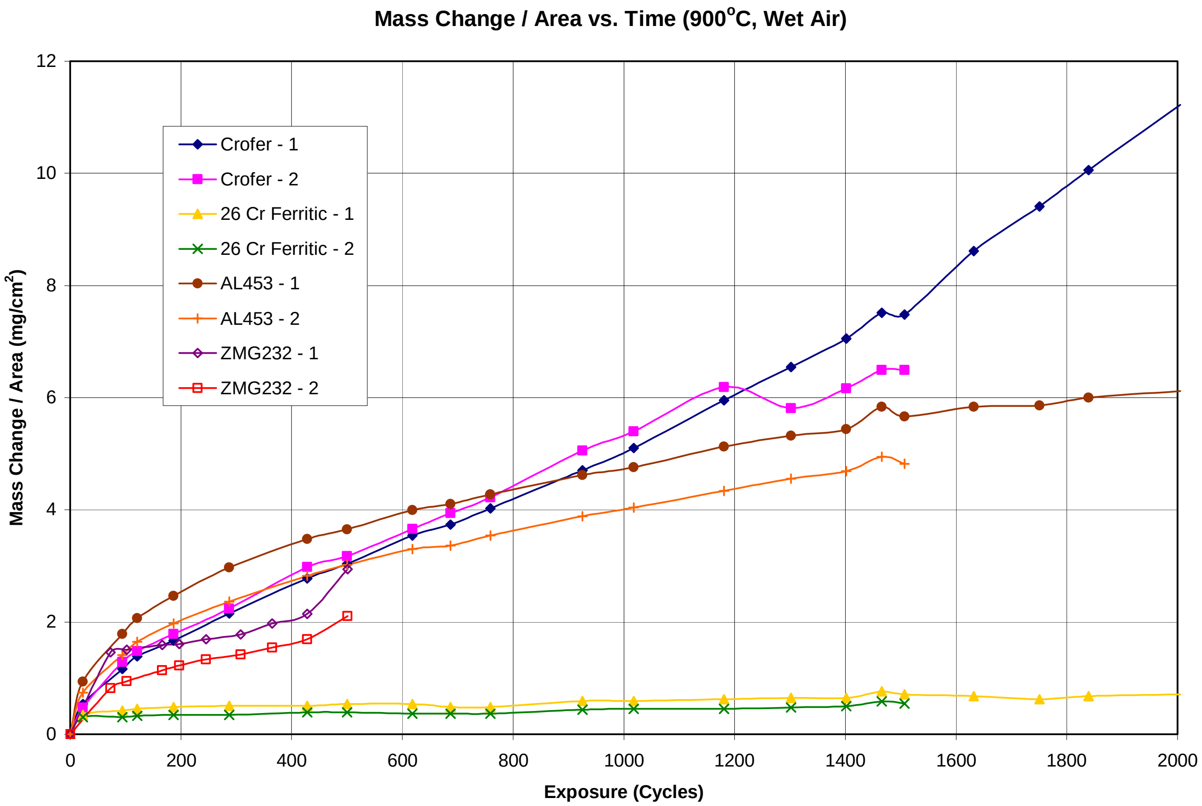

Figure 49: Mass Change vs. Exposure Time for Samples at 900°C in Air + 0.1 atm H_2O (data for Crofer, 26 Cr Ferritic, and AL453 from Reference 31, data for ZMG232 from own research)

Figure 50 shows the micrograph for Crofer after 2005 hours. There is a small amount of internal oxidation of aluminum below the surface, and a thin layer of manganese chromate above the chromia layer. The cross-sectional micrograph of 26 Cr Ferritic after 2005 hours is shown in Figure 51. Just below the oxide layer is an area of silicon rich oxides. Also, internal oxidation of aluminum has occurred and can be seen below the chromia scale. Figure 52 shows the micrograph of the cross-section of AL453 after 2005 hours. Again, aluminum has internally oxidized and can be seen below the chromia scale. There is also a metal layer between the oxide layer and the internal oxidation zone. The micrograph for ZMG232 after 501 hours is shown in Figure 53. A manganese chromate layer can be observed above the chromia scale. Aluminum has internally oxidized and can be seen below the surface. An area of silicon rich oxides has formed just beneath the oxide layer. There is also a silicon carbide inclusion that is rich in aluminum and oxygen. Around this inclusion is an area of chromia rich in aluminum, silicon, and oxygen.

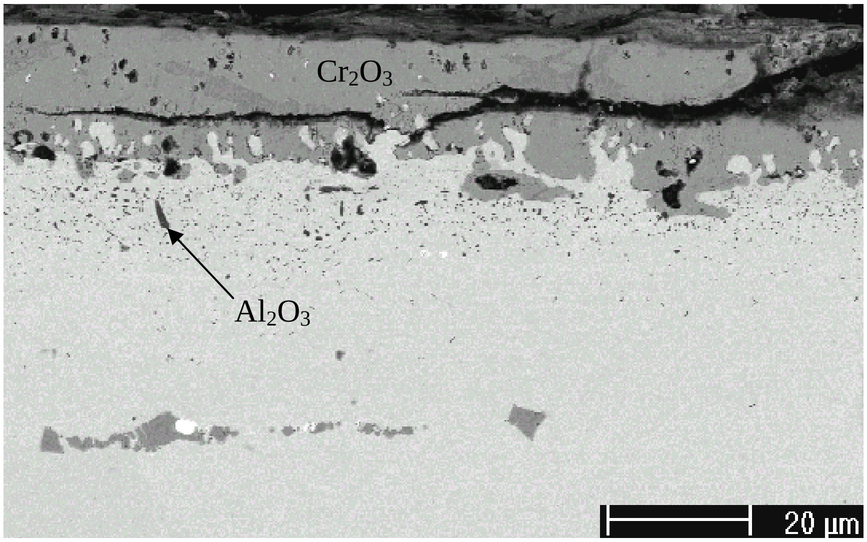

Figure 50: Crofer exposed at 900°C in Air + 0.1 atm H_2O for 2005 hours (from Reference 31)

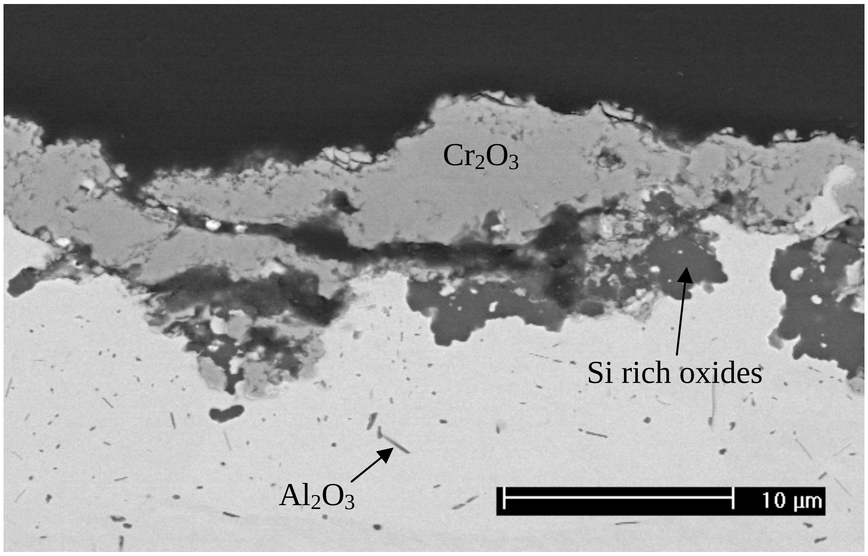

Figure 51: 26 Cr Ferritic exposed at 900°C in Air + 0.1 atm H_2O for 2005 hours (from Reference 31)

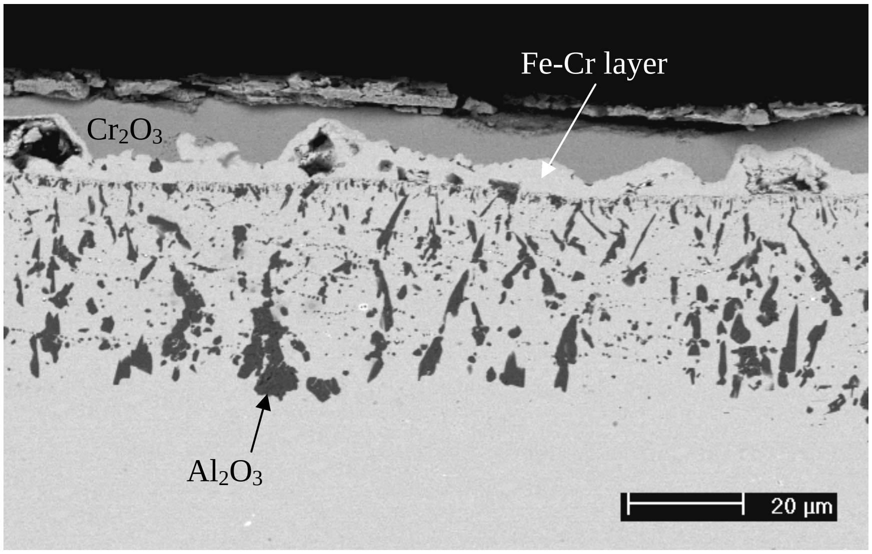

Figure 52: AL453 exposed at 900°C in Air + 0.1 atm H_2O for 2005 hours (from Reference 31)

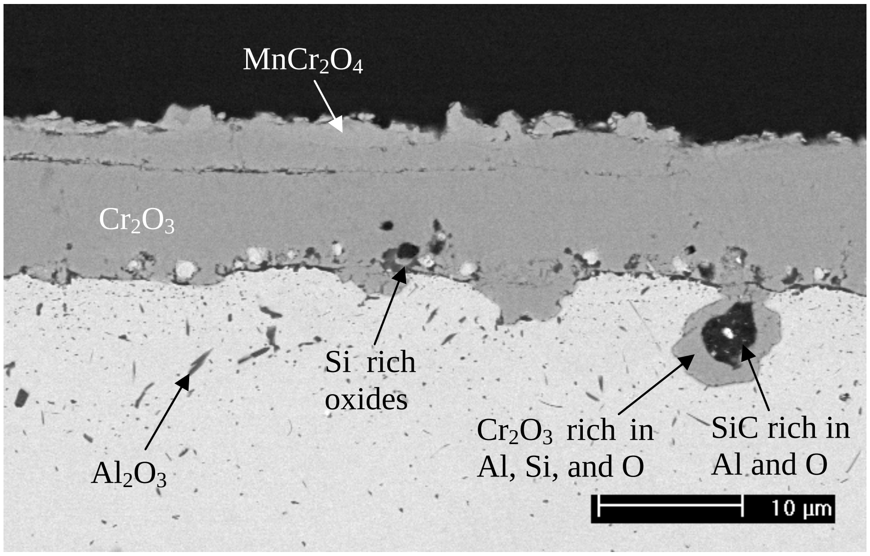

Figure 53: ZMG232 exposed at 900°C in Air + 0.1 atm H_2O for 501 hours

3.1.8 Discussion of Error

An error analysis is not possible with the oxidation tests that were performed. The weight change data can accurately be measured to about plus or minus 0.1 mg. Factors that enter into the error include vaporization of the oxide, variation of oxide growth for oxide layers of different thicknesses, spallation of the oxide, and transient oxide growth in the spalled areas. Also, for the alloys in which internal oxidation has occurred, the features of the internal oxide vary in ways that are difficult to analyze. Duplicate tests are performed to account for these variables. As the temperature increases, the reproducibility increases as well. The mass changes at 700°C were the smallest, but the reproducibility was the worst. At 900°C, though, the mass changes were the largest and the reproducibility was the best.

3.1.9 Discussion of Oxidation Results

At 700^{o}C, most of the alloys studied (Crofer, 26 Cr Ferritic, AL453, Modified AL453, and ZMG232) were chromia-formers. The exception is nickel, which of course formed nickel oxide. Crofer that had been exposed in air + 0.1 atm H_2O had the smallest mass gains, followed by dry air, and then in $Ar/H_2/H_2O$ which produced the largest mass gains. The smallest mass gains for 26 Cr Ferritic occurred in air + 0.1 atm H_2O, followed by dry air, and then the largest which was in $Ar/H_2/H_2O$. AL453 had the smallest mass gains in air + 0.1 atm H_2O, followed by dry air, and then $Ar/H_2/H_2O$. The mass gains for Modified AL453 in dry air were smaller than those obtained when exposed in air + 0.1 atm H_2O. ZMG232 in air + 0.1 atm H_2O had smaller mass gains than in dry air. The mass gains for nickel that had been exposed in $Ar/H_2/H_2O$ were smaller than those in air + 0.1 atm H_2O.

For Crofer, 26 Cr Ferritic, and AL453 the smallest mass gains occurred in air + 0.1 atm H_2O, followed by dry air, and then $Ar/H_2/H_2O$. This can be explained by considering that spallation will greatly be increased by the presence of water vapor, which will cause mass losses. Also, the vaporization of CrO_3 is more prevalent in water vapor. This too will cause mass losses. The largest mass gains for these alloys were in $Ar/H_2/H_2O$ since larger mass gains are observed in H_2/H_2O mixtures. This is because the reduced partial pressures of oxygen in H_2/H_2O mixtures allow for minimal mass losses from chromia evaporation[32]. The mass gains for Modified AL453 that had been exposed in dry air were smaller than the mass gains in air + 0.1 atm H_2O. An explanation for this is that the presence of water vapor often increases the oxidation kinetics, causing a larger mass gain than if there was no water vapor present. ZMG232 in air + 0.1 atm H_2O had smaller mass gains than when exposed to dry air. This is because water vapor often can increase the spallation of alloys and the metal can be consumed. It is also possible that chromia evaporation occurred more readily in the air + 0.1 atm H_2O. The mass gains for nickel in $Ar/H_2/H_2O$ were smaller than the mass gains in air + 0.1 atm H_2O. This is because there is a higher oxygen partial pressure in air + 0.1 atm H_2O than in $Ar/H_2/H_2O$. In fact, the partial pressure of oxygen in the $Ar/H_2/H_2O$ atmosphere is too low to oxidize nickel.

For samples that had been exposed at 700^oC in $Ar/H_2/H_2O$, nickel had the smallest mass gains, followed by 26 Cr Ferritic (oxide thickness is 0.55 µm), Crofer (oxide thickness is 1.5 µm), and AL453 (oxide thickness is 1.3 µm). Generally speaking, the smaller the mass gain is, the thinner the oxide layer will be. This is only a general rule because factors such as the amount of internal oxidation or silica formation below the oxide can affect this. AL453 had the largest mass gain, but not the thickest oxide layer. A continuous layer of alumina has formed just beneath the oxide layer of this sample (Figure 16), which could be one possible reason for the discrepancy about AL453 having the largest mass gain but not the thickest oxide.

For alloys oxidized in dry air at 700^oC, Modified AL453 (oxide thickness is 0.5 µm) had the smallest mass gains, followed by 26 Cr Ferritic (oxide thickness is 0.75 µm), Crofer (oxide thickness is 1.75 µm), AL453 (oxide thickness is 0.5 µm), and ZMG232 (oxide thickness is 4.25 µm). Internal oxidation of aluminum has occurred with the AL453 sample (Figure 20), and the internal alumina will increase the mass. This is the reason that AL453 has one of the thinnest oxide scales but one of the largest mass gains.

In air + 0.1 atm H_2O at 700^oC, 26 Cr Ferritic (oxide thickness is 0.5 µm) had the smallest mass gains, followed by Modified AL453 (oxide thickness is 0.5 µm), ZMG232 (oxide thickness is 1.4 µm), Crofer (oxide thickness is 1 µm), and AL453 (oxide thickness is 0.8 µm). The specimen of Crofer that had been exposed at 700^oC in air + 0.1 atm H_2O contained both internal alumina and internal silica (Figure 25). More alumina and silica were present than in the other atmospheres at 700°C. For the AL453 sample (Figure 27), an almost continuous layer of alumina has formed beneath the chromia scale. The presence of the alumina and silica in the Crofer sample and alumina in the AL453 sample are the reasons that these alloys have oxide thicknesses that are inconsistent with the mass change data.

Most of the alloys studied at 800°C were chromia formers (JS-3, Crofer, new Crofer, E-brite, and 26 Cr Ferritic). The only exception was Type 304 stainless steel, which had an oxide layer that consisted mainly of iron rich oxides. At this temperature, testing was only performed in air + 0.1 atm H_2O, so comparisons that are similar to those made at 700°C for each alloy in different environments cannot be made here.

Under exposure conditions of 800°C and air + 0.1 atm H_2O, Type 304 stainless steel (oxide thickness is 5.75 μm – after 168 hours) had the smallest mass gains. This was followed by 26 Cr Ferritic (oxide thickness is 2.2 μm – after 992 hours), E-brite (oxide thickness is 0.65 μm – after 992 hours), JS-3 (oxide thickness is 1.4 μm), New Crofer (oxide thickness is 2.1 μm), and finally Crofer (oxide thickness is 3.1 μm). Type 304 stainless steel (Figure 39) had the thickest oxide and smallest mass gain after the shortest amount of exposure time. One possible reason for this could be that the chromia that was present was rich in manganese and iron. Also, an oxide rich in nickel, chromium, and iron and an iron oxide rich in nickel, chromium, and manganese were present on the surface. These multiple oxides grow rapidly and affect the mass change data. It is also likely that spallation occurred and caused the 304 stainless steel to lose mass.

At 900°C, the alloys studied (Crofer, 26 Cr Ferritic, AL453, and ZMG232) were again chromia-formers, but the weight gains were much larger than those that were observed at 700°C. The smallest mass gains for Crofer were in dry air, followed by $Ar/H_2/H_2O$, and then the largest which was in air + 0.1 atm H_2O. 26 Cr Ferritic had the smallest mass gains in air + 0.1 atm H_2O, followed by dry air, and then $Ar/H_2/H_2O$. AL453 that had been exposed in dry air had the smallest mass gains, followed by $Ar/H_2/H_2O$, and then air + 0.1 atm H_2O. The mass gains for ZMG232 in air + 0.1 atm H_2O were smaller than those obtained when exposed in dry air.

The mass gains for Crofer and AL453 were smallest in dry air, followed by $Ar/H_2/H_2O$, and then air + 0.1 atm H_2O. These weight changes cannot be accounted for in detail, but higher combined partial pressures of oxygen and water vapor will give larger mass gains. For 26 Cr Ferritic, the smallest mass gains occurred when oxidized in air + 0.1 atm H_2O, followed by dry air, and then $Ar/H_2/H_2O$ which produced the largest mass gains. Water vapor can increase the amount of spallation, which will consume metal and cause mass losses. Larger mass gains are observed in H_2/H_2O mixtures, so the largest mass gains were for the case where 26 Cr Ferritic was oxidized in $Ar/H_2/H_2O$. Minimal mass losses from chromia evaporation occurred because of the reduced oxygen partial pressures in H_2/H_2O mixtures[32]. The mass gains for ZMG232 that had been exposed in air + 0.1 atm H_2O were smaller than the mass gains in dry air. This is because the presence of water vapor often can increase the spallation of alloys, and in some areas on the ZMG232 sample that had been exposed in air + 0.1 atm H_2O, the manganese chromate layer has spalled. Due to a lack of a protective oxide layer in some places on the alloy, chromia evaporation can occur.

At 900^oC and in $Ar/H_2/H_2O$, Crofer (oxide thickness is 8 μm) had the smallest mass gains, followed by 26 Cr Ferritic (oxide thickness is 9 μm), and lastly AL453 (oxide thickness is 4.5 μm). AL453 had the largest mass gain, but the thinnest oxide layer. In the micrograph for AL453 at 900^oC in $Ar/H_2/H_2O$ (Figure 43), a large amount of internal oxidation has been observed, which contributes to the weight of the specimen. This is the reason for the large mass gain and relatively thin oxide layer for this sample.

For alloys exposed in dry air at 900^{o}C, 26 Cr Ferritic (oxide thickness is 7.5 µm) had the smallest mass gains, followed by Crofer (oxide thickness is 13 µm), AL453 (oxide thickness is 6 µm), and ZMG232 (oxide thickness is 12.5 µm – after 501 hours). Aluminum has internally oxidized in the AL453 sample (Figure 47), and the internal alumina will increase the mass. This is the reason that AL453 has the thinnest oxide scale but close to the largest mass gain.

In air + 0.1 atm H_2O at 900^{o}C, 26 Cr Ferritic (oxide thickness is 11.5 µm) had the smallest mass gains, followed by ZMG232 (oxide thickness is 12 µm – after 501 hours), AL453 (oxide thickness is 8.5 µm), and Crofer (oxide thickness is 20 µm). As in the previous cases, internal oxidation of aluminum has occurred with the AL453 sample (Figure 52). The internal alumina will increase the mass and is the reason that AL453 has the thinnest oxide scale but one of the largest mass gains.

The amount of chromium that is present in the alloys will determine how good of a chromia-former they are and the amount of oxidation resistance that they possess. Type 304 stainless steel has the lowest concentration of chromium (18 – 20 percent) and therefore is the poorest at forming chromia on the surface. Its resistance to oxidation is also the lowest of the chromia-forming alloys studied. The remaining alloys (except for nickel) have similar oxidation kinetics. Crofer has the next lowest chromium concentration (20 – 24 percent), followed by AL453 and ZMG232 (both with 22 percent), JS-3 (23 percent), and then E-brite and 26 Cr Ferritic (both with approximately 26 percent). In the alloys that contain greater than 20 percent chromium, a protective chromia scale is formed on the surface. The specific oxide behavior is determined by the amounts of chromium and manganese. The more chromium that is present in the alloy, the more likely it is that chromium will selectively oxidize. There will not necessarily be a greater resistance to oxidation though because chromia vaporization can occur. The presence of manganese forms an outer layer of $MnCr_2O_4$ and will inhibit the vaporization of chromia.

Internal subscales form below the chromia scales in the alloys that contain silicon and aluminum and contribute to the weight increase of the specimens. When the silicon and aluminum contents are sufficiently high, continuous silica and alumina layers can develop. These continuous layers improve the oxidation behavior and cause high ASR values. In some cases (AL453 at 700°C in dry air – Figure 20, AL453 at 700°C in air + 0.1 atm H_2O – Figure 27, AL453 at 900°C in $Ar/H_2/H_2O$ – Figure 43, AL453 at 900°C in dry air – Figure 47, and AL453 at 900°C in air + 0.1 atm H_2O – Figure 52), the internal oxides can cause extrusion of the alloy which results in a zone consisting of the alloy above the internal oxidation zone and below the chromia scale. The average composition of the extruded metal layer is 68% iron, 16% chromium, 1% silicon, 9% aluminum, and 5% oxygen. The metal layer composition was found using EDX on the SEM. Measurements taken this way are only accurate to the ones place, hence the lack of decimals in these measurements. When compared to the amounts of these elements that are present in AL453 (76.3% iron, 22.0% chromium, 0.3% silicon, 0.6% aluminum, and 0.0% oxygen), there is less iron, less chromium, more silicon, more aluminum, and more oxygen in the extruded metal layer than in the alloy.

Alloy extrusion occurs because an increase in volume is associated with the formation of internal oxide precipitates. It is possible for high compressive stresses to be created due to the large change in volume. These compressive stresses occur both within the internal oxidation zones and at the internal oxidation front[33]. A stress gradient arises between the surface region, which is free of stress, and the internal oxidation front, which is under a compressive stress. Ag-In alloys were studied, and it was found that the diffusional transport of silver to the surface was responsible for the stress relief in these alloys. The volume of silver nodules that formed on the surface was equivalent to the increase in volume from the internal oxidation of indium[34]. Even though these results are from an investigation in which Ag-In alloys were studied, the results hold for any alloy. Also, in this investigation, no oxide scale formed on the surface, but for cases in which there is an oxide scale, the extruded alloy will form below the oxide layer.

3.2 SIGMA PHASE EXPERIMENTS

Figure 54 shows the XRD pattern for a 26 Cr Ferritic sample exposed for 2000 hours at 700°C in air + 0.1 atm H_2O. Many of the peaks match with the chromia lines, the iron-chromium lines, or the sigma phase lines. This analysis proved that the sample did in fact contain the sigma phase.

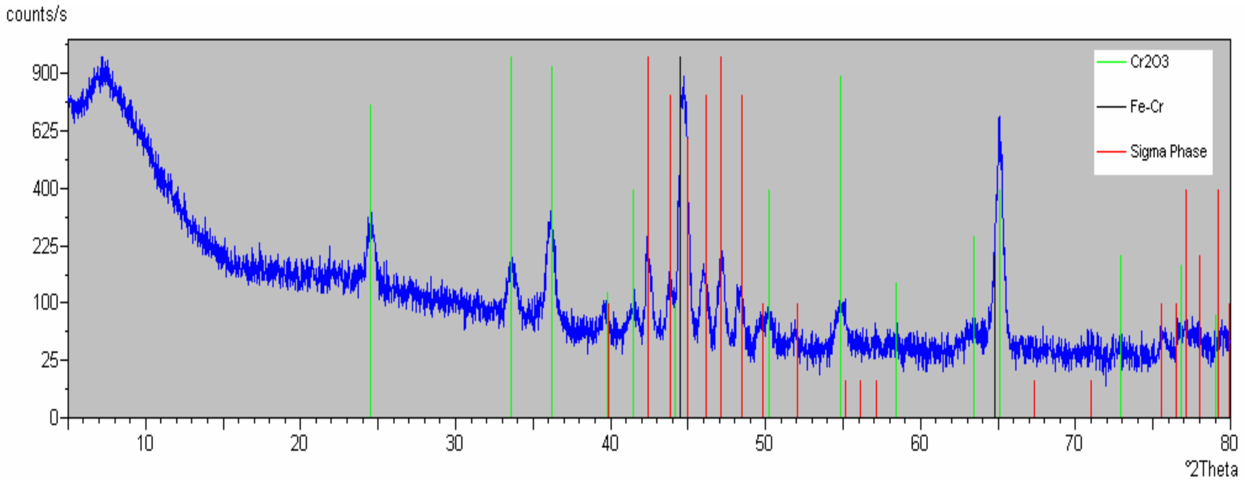

Figure 54: X-ray Diffraction Pattern for 26 Cr Ferritic Sample exposed at 700°C in Air + 0.1 atm H_2O for 2000 hours

The compositions of the sigma phase and the ferrite in the affected zone were found using EDX on the SEM and are shown in Table 8. From the table, it can be seen that the average composition of the sigma phase is 59% iron, 35% chromium, and 4% molybdenum. The average composition of the ferrite in the affected zone is 73% iron, 24% chromium, and 2% molybdenum. There is less iron, more chromium, and more molybdenum in the sigma phase than in the surrounding areas. The EDX measurements are only accurate to the ones place, hence the lack of decimals in these measurements.

Table 8: Compositions of Sigma Phase and Ferrite in Affected Zone

Atmosphere	Exposure Time (hrs)	Composition of Sigma Phase			Composition of Ferrite in Affected Zone		
		wt% Fe	wt% Cr	wt% Mo	wt% Fe	wt% Cr	wt% Mo
Dry Air	2000	58	36	5	71	26	2
Wet Air	2000	58	37	4	72	25	2
SAG	2000	63	33	3	76	22	1
Average		59	35	4	73	24	2

Figure 55 shows E-brite that had been exposed in dry air at 700^{o}C in 50 hour increments to 500 hours. Only a small amount of the sigma phase is seen after 200 hours, but with time, more is seen in each successive micrograph.

The micrographs of 26 Cr Ferritic after being exposed in dry air at 700^{o}C in 50 hour increments up to 500 hours are shown in Figure 56. Again, there is only a small amount of sigma phase observed in the sample exposed for 200 hours. As the exposure time is increases, the amount of sigma phase also increases.

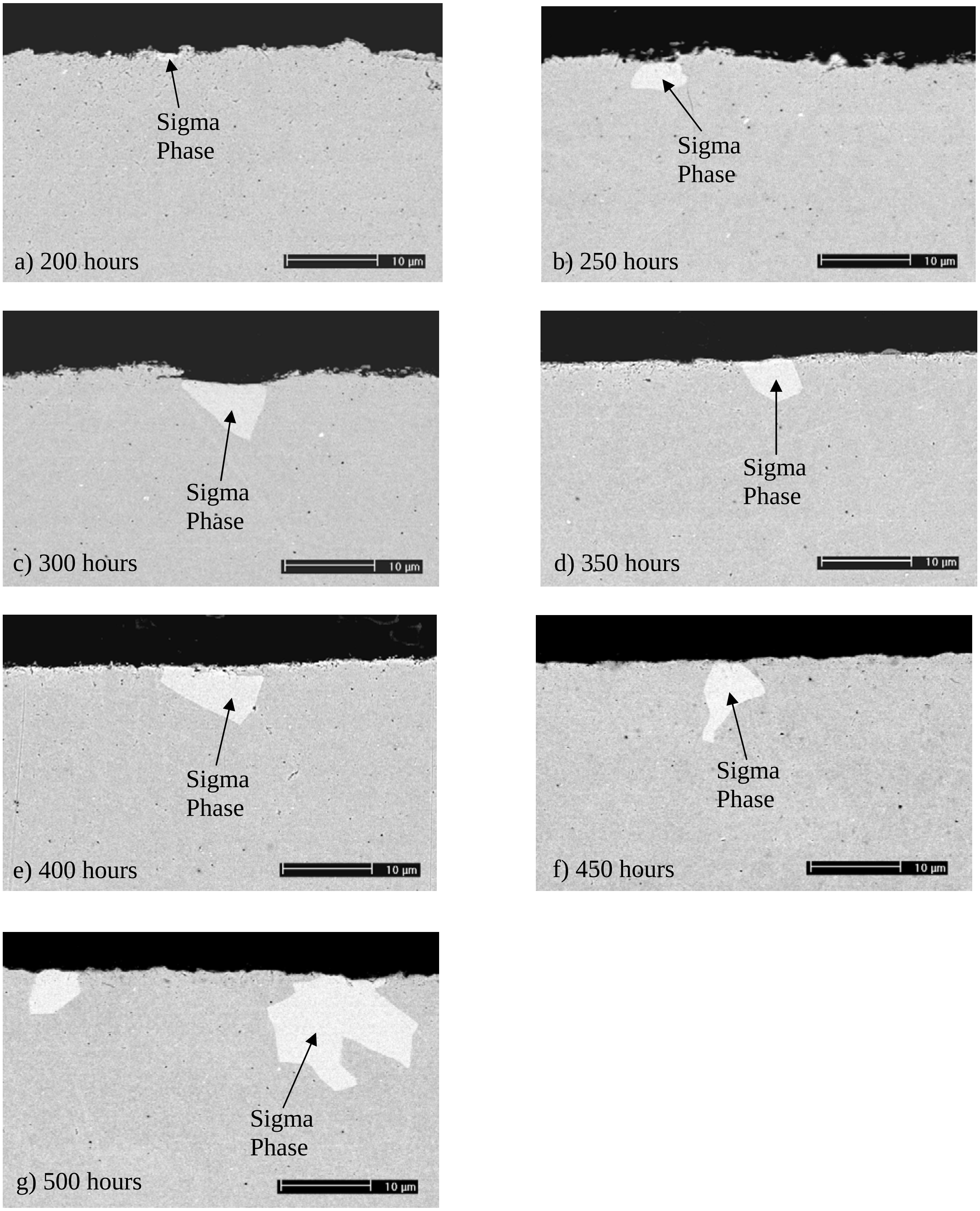

Figure 55: E-brite exposed at 700°C in Dry Air in 50 hour increments after a) 200 hours, b) 250 hours, c) 300 hours, d) 350 hours, e) 400 hours, f) 450 hours, and g) 500 hours

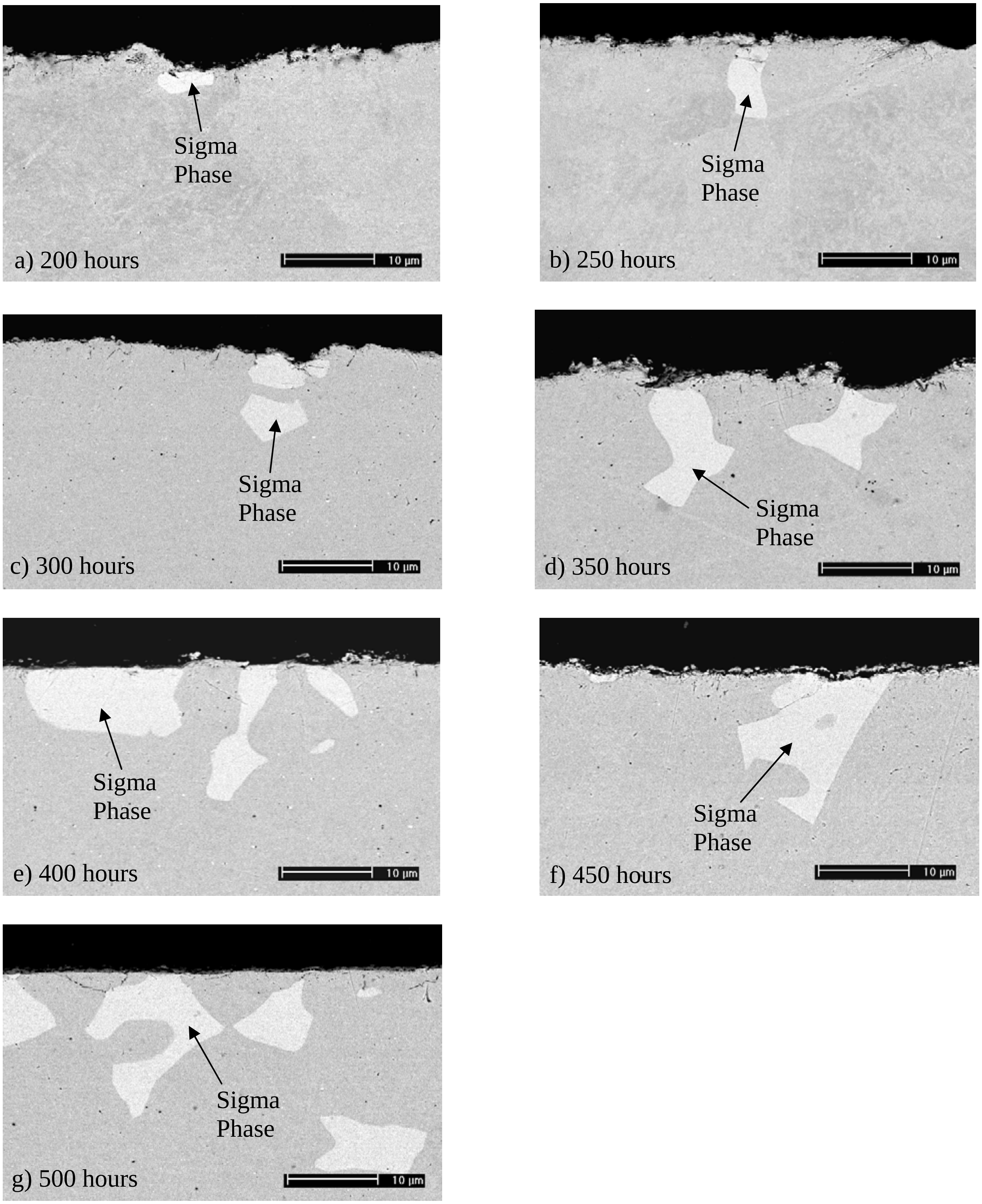

Figure 56: 26 Cr Ferritic exposed at 700°C in Dry Air in 50 hour increments after a) 200 hours, b) 250 hours, c) 300 hours, d) 350 hours, e) 400 hours, f) 450 hours, and g) 500 hours

3.2.1 Discussion of Sigma Phase Experiment Results

E-brite contains 1.0% molybdenum and 0.2% silicon. 26 Cr Ferritic contains 2% molybdenum and 0.2% silicon. Additions of molybdenum and silicon will increase the rate of sigma phase formation[27], but because 26 Cr Ferritic contains a larger combined amount of molybdenum and silicon than E-brite, it will more easily form the sigma phase. This is what was observed with the experiments that were performed to determine the amount of sigma phase that forms in these two alloys.

The sigma phase was observed only in 26 Cr Ferritic that had been exposed at 700^{o}C in the three atmospheres that were studied. Figure 57 shows a micrograph of 26 Cr Ferritic that had been exposed in Ar/H_2/H_2O for 2000 hours. In this sample, the sigma phase has formed throughout the sample, but mostly it has formed through approximately 75µm. The micrograph of 26 Cr Ferritic after 2000 hours in dry air is shown in Figure 58. The sigma phase has formed through about 65µm. Figure 59 shows 26 Cr Ferritic after exposure in air + 0.1 atm H_2O for 2000 hours, and sigma has formed throughout the sample. Cracks were found in the sigma phase in the three environments studied (see Figure 60).

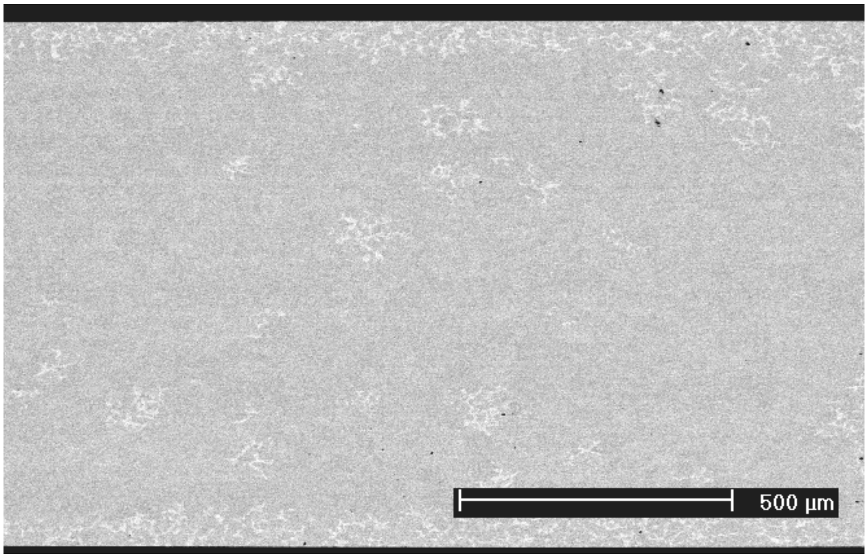

Figure 57: 26 Cr Ferritic exposed at 700°C in Ar/H_2/H_2O for 2000 hours and showing that the sigma phase formed throughout the sample

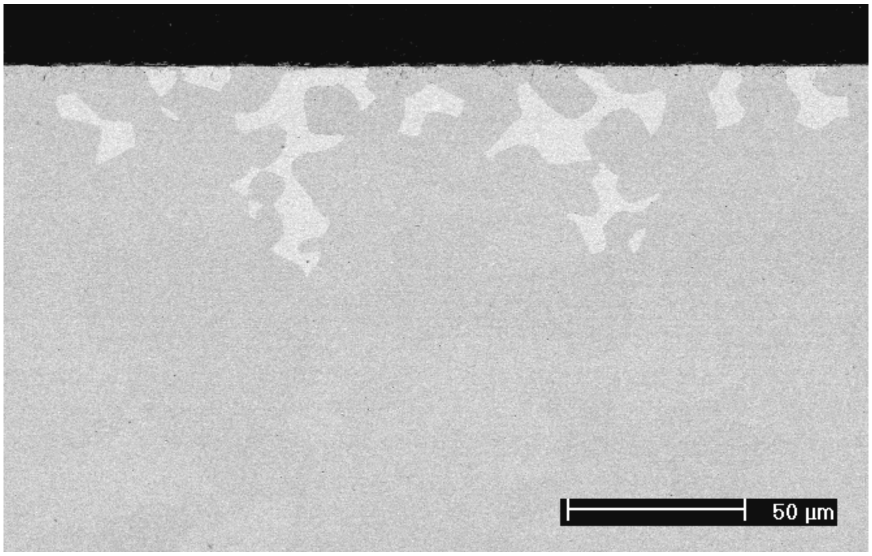

Figure 58: 26 Cr Ferritic exposed at 700°C in Dry Air for 2000 hours and showing that the sigma phase formed near the surface

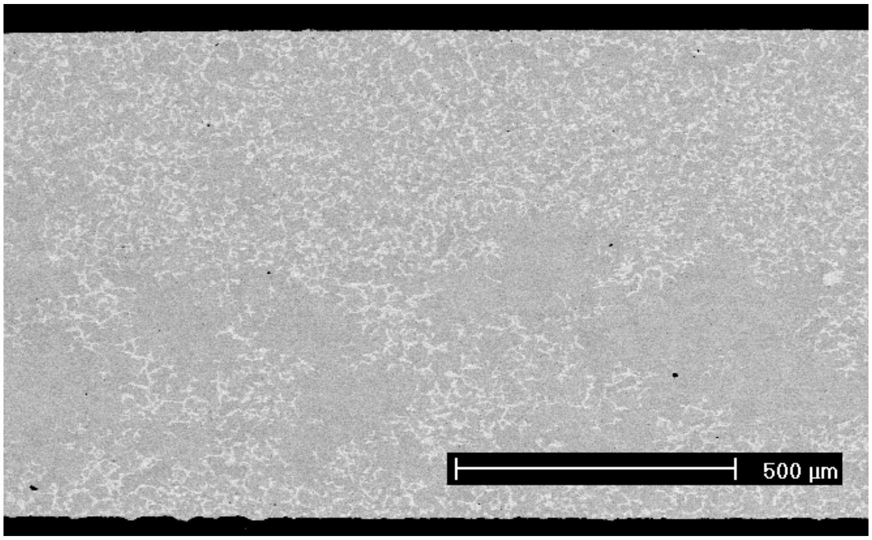

Figure 59: 26 Cr Ferritic exposed at 700°C in Air + 0.1 atm H_2O for 2000 hours and showing that the sigma phase formed throughout the sample

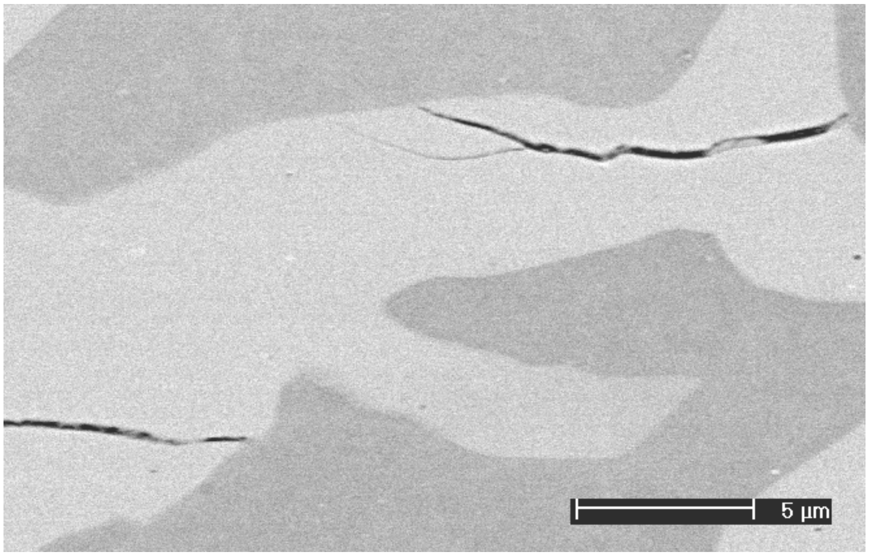

Figure 60: Cracks that have formed in the sigma phase

The sigma phase formed the slowest in dry air. It developed faster in the gases that contained water vapor. The $Ar/H_2/H_2O$ environment had sigma form faster than in dry air, but the air + 0.1 atm H_2O was the fastest. The sigma phase also tended to nucleate at the surface and grow inward.

The reason that the sigma phase was only observed at 700^{o}C can be explained if the Fe-Cr phase diagram is examined (see Figure 61). E-brite and 26 Cr Ferritic both contain approximately 26% chromium, which is more than the other alloys that were investigated. In Figure 61, point A (700^{o}C, 26% chromium) is within the region where sigma forms, but point B (900^{o}C, 26% chromium) is outside of this region. E-brite and 26 Cr Ferritic that are cooled from 800^{o}C or 900^{o}C do not form the sigma phase, even though they pass through a region on the phase diagram that can form it. This is because the sigma phase forms slowly and, for most of the time, the alloys are outside the phase field in which sigma will form.

The composition of the sigma phase only contained 35% chromium, but according to the phase diagram (Figure 61), there should be approximately 45% chromium. This discrepancy comes about because the composition according to the phase diagram is only accurate when only iron and chromium are present. The other elements present in these alloys, particularly molybdenum, affect the phase diagram and therefore the composition of the sigma phase.

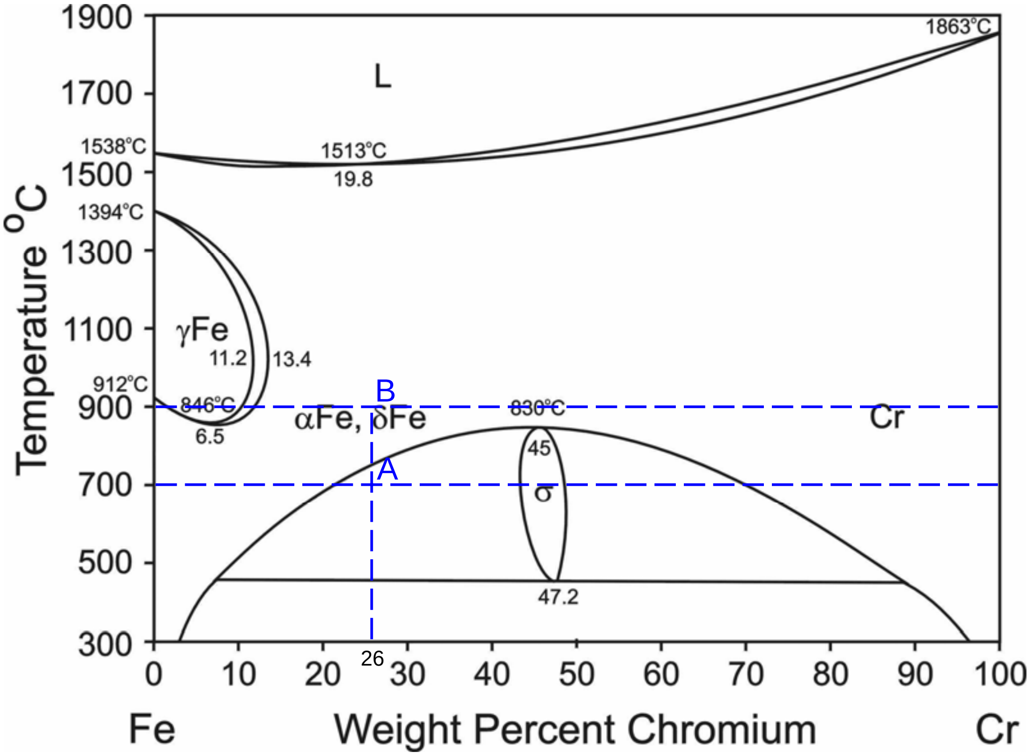

Figure 61: The Fe-Cr Phase Diagram used to explain the reason for which sigma forms only in E-brite and 26 Cr Ferritic at 700°C

3.3 CONDUCTIVITY

Figure 62 shows the ASR vs. Temperature for some of the alloys that were exposed at 900°C in $Ar/H_2/H_2O$, dry air, or air + 0.1 atm H_2O. The oxide layer on the alloys needed to be continuous (for example, no spalling could have occurred) for the ASR to be measured. This is why only some of the alloys at 900°C were tested.

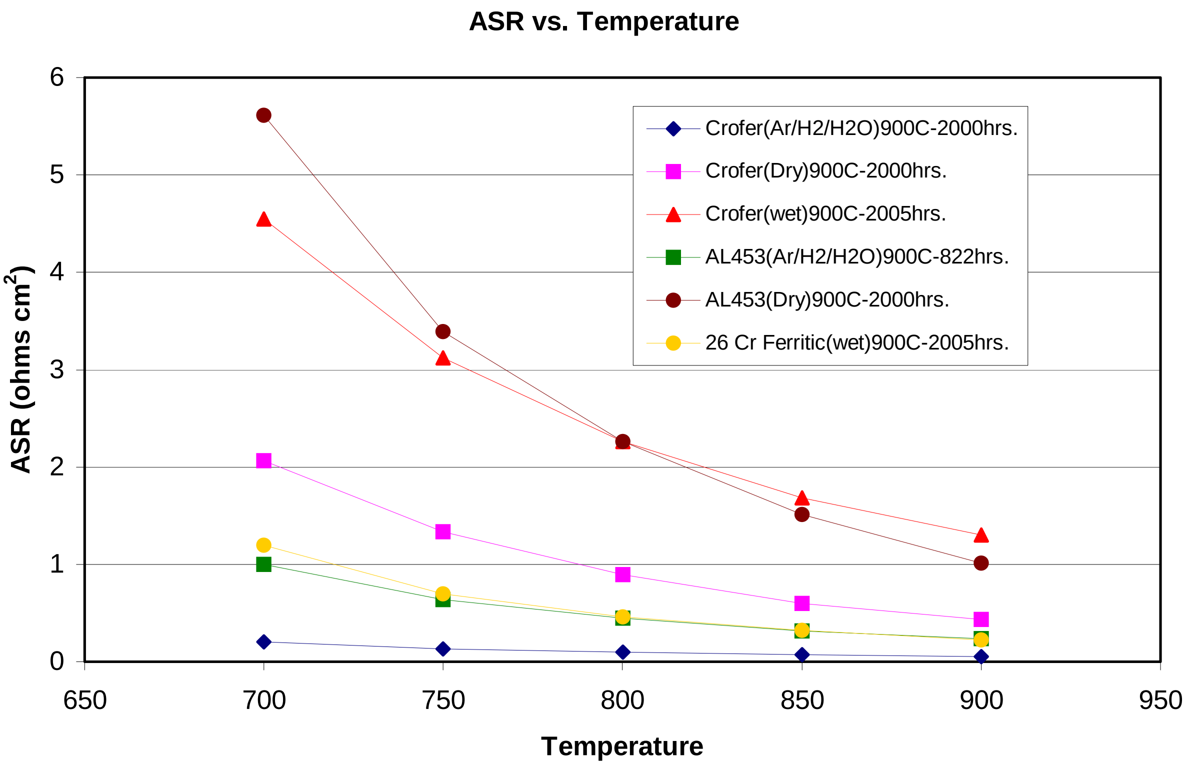

Figure 62: ASR vs. Temperature

The ASR values at 700°C and 900°C and the corresponding oxide thicknesses are shown below in Table 9.

Table 9: ASR Values and Oxide Thicknesses at 700°C and 900°C for Selected Alloys

Sample	ASR at 700°C (ohms cm^2)	ASR at 900°C (ohms cm^2)	Oxide Thickness (μm)	Average Thickness (μm)
Crofer, $Ar/H_2/H_20$, 900°C, 2000 hrs	0.204	0.054	5-11	8
Crofer, dry air, 900°C, 2000 hrs	2.061	0.435	11-15	13
Crofer, air + 0.1atm H_2O, 900°C 2005 hrs	4.550	1.301	14-26	20
AL453, $Ar/H_2/H_2O$, 900°C, 822 hrs	0.996	0.237	2-5	3.5
AL453, dry air, 900°C, 2000 hrs	5.612	1.015	4-8	6
26 Cr Ferritic, air + 0.1atm H_2O, 900°C 2005 hrs	1.193	0.222	8-15	11.5

3.3.1 Discussion of Conductivity Results

At 700°C, the largest ASR value was for AL453 in dry air that was exposed at 900°C for 2000 hours (average oxide thickness is 6μm), followed by Crofer in air + 0.1 atm H_2O at 900°C for 2005 hours (average oxide thickness is 20μm), Crofer in dry air at 900°C for 2000 hours (average oxide thickness is 13μm), 26 Cr Ferritic in air + 0.1 atm H_2O at 900°C for 2005 hours (average oxide thickness is 11.5μm), AL453 in $Ar/H_2/H_2O$ at 900°C for 822 hours (average oxide thickness is 3.5μm), and Crofer in $Ar/H_2/H_2O$ at 900°C for 2000 hours (average oxide thickness is 8μm).

At 900°C, Crofer in air + 0.1 atm H_2O that was exposed at 900°C for 2005 hours (average oxide thickness is 20μm) had the largest ASR value. This was followed by AL453 in dry air at 900°C for 2000 hours (average oxide thickness is 6μm), Crofer in dry air at 900°C for 2000 hours (average oxide thickness is 13μm), AL453 in $Ar/H_2/H_2O$ at 900°C for 822 hours (average oxide thickness is 3.5μm), 26 Cr Ferritic in air + 0.1 atm H_2O at 900°C for 2005 hours (average oxide thickness is 11.5μm), and Crofer in $Ar/H_2/H_2O$ at 900°C for 2000 hours (average oxide thickness is 8μm).

All of the ASR values obtained from conductivity tests performed at 700^{o}C and 900^{o}C are larger than the required value of 0.01 ohm cm^2. Additionally for both temperatures, as there is a decrease in ASR, the thicknesses of the oxides roughly decrease as well.

3.4 STRESS MEASUREMENTS

Figure 63 shows the $\sin^2\psi$ plot for Crofer exposed in dry air at 900°C for 100 cycles using the 220 lattice plane. The stresses in the scale had a value of -2.19 GPa.

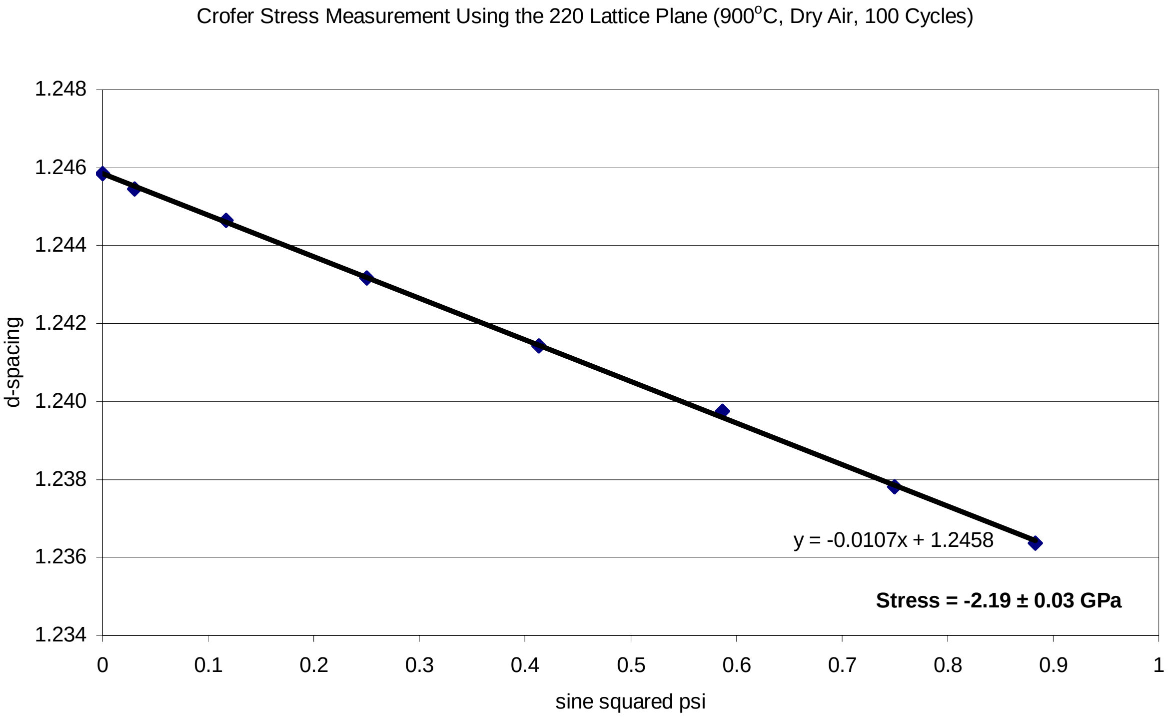

Figure 63: The $\sin^2\psi$ plot for Crofer exposed at 900°C for 100 cycles in dry air

The $\sin^2\psi$ plot for Crofer exposed in air + 0.1 atm H_2O at 900°C for 100 cycles using the 416 lattice plane is shown in Figure 64. The stresses in the scale had a value of -2.06 GPa.

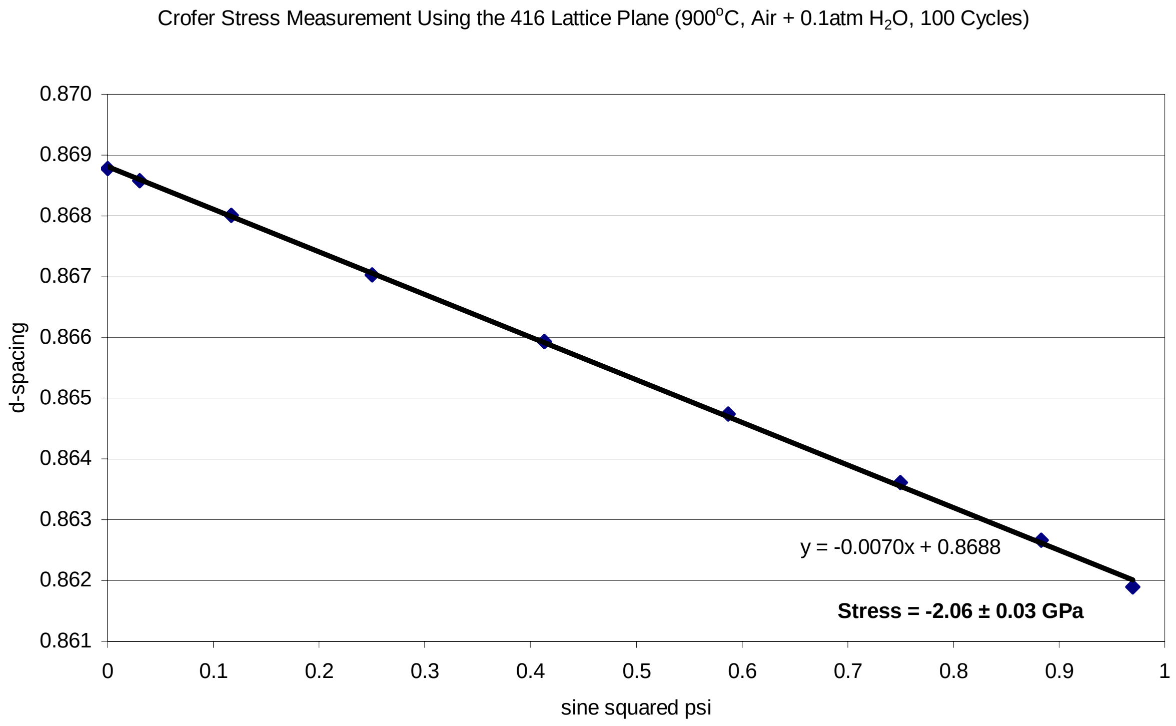

Figure 64: The sin$^2\psi$ plot for Crofer exposed at 900°C for 100 cycles in air + 0.1 atm H_2O

3.4.1 Discussion of Stress Measurement Results

Equations for determining the stresses in chromia were given in Section 2.4. Using these equations and knowing the values for Young's Modulus (E = 314.42 GPa) and Poisson's ratio (ν = 0.28), the stresses can be found.

The Crofer sample that had been exposed in dry air at 900°C for 100 cycles using the 220 lattice plane had a stress of -2.19 GPa. The stress found in Crofer exposed in air + 0.1 atm H_2O at 900^{o}C for 100 cycles using the 416 lattice plane had a value of -2.06 GPa. These values can be compared with the calculated thermal stresses for chromia of -2.22 GPa. The stresses that were determined by the stress measurements compare reasonably well with the calculated thermal stresses for chromia. This means that either there were no growth stresses or the alloy relaxed by creep.

4.0 CONCLUSIONS

This study consisted only of experiments performed in a single atmosphere. Because a fuel cell operates in a dual atmosphere environment, these results can be thought of as a baseline for experiments that will be carried out in dual atmospheres.

It is a bit difficult to compare the oxidation behavior of the alloys studied at the temperatures and environments in question because at least three processes have occurred at the same time. The oxide scale has grown, some spalling of the oxide has taken place due to the temperature changes brought about from cycling, and chromia vaporization has occurred to various degrees.

At 700^{o}C, the mass changes for the alloys in the three environments studied are not considerably different. These values vary from about -0.08 mg/cm^2 for 26 Cr Ferritic in air + 0.1 atm H_2O to 0.62 mg/cm^2 for AL453 in $Ar/H_2/H_2O$, excluding nickel, which has a mass gain of 2.46 mg/cm^2 in air + 0.1 atm H_2O. The 26 Cr Ferritic alloy is always at the low range of the mass change data and mass losses are observed in air + 0.1 atm H_2O. Even though this alloy contains manganese, the small mass gains or mass losses may be due to chromia vaporization. This is because spallation may have occurred and removed the manganese chromate layer, thereby allowing evaporation of chromia to occur. Small mass gains have also been obtained for the Modified AL453 alloy. This is most likely because of the pretreatment that had been applied to this alloy. AL453 is always at the upper range of mass change data. This is due to the relatively large amount of silicon and aluminum that is present in this alloy. Also, a large amount of internal alumina has formed in AL453 in all three environments, and the formation of these particles could increase the mass gain. At 700^{o}C, Crofer and ZMG232 appear to have the best oxidation behavior for use in fuel cells. Both alloys form a manganese chromate layer above the chromia scale, and there is a small amount of alumina and silica below the surface compared to the other alloys at this temperature. 26 Cr Ferritic also has a minimal amount of internal alumina and silica. However, it does not form a manganese chromate layer, and the sigma phase is present in this alloy.

At 800^{o}C, the only atmosphere studied was air + 0.1 atm H_2O. The mass changes varied from about -0.06 mg/cm^2 for E-brite and 26 Cr Ferritic to 0.61 mg/cm^2 for Crofer, excluding Type 304 stainless steel, which has a mass loss of -11.12 mg/cm^2. Mass losses were observed for Type 304 stainless steel, E-brite, and 26 Cr Ferritic. Spallation occurred with Type 304 stainless steel and is the reason for the mass loss. For the E-brite and 26 Cr Ferritic alloys, vaporization of chromia is the reason mass losses were observed. E-brite and 26 Cr Ferritic both contain manganese, and therefore a manganese chromate layer can form. In some cases, however, this layer has spalled, and chromia vaporization is not completely prevented. The JS-3, Crofer, and New Crofer alloys behave similarly, but Crofer has larger mass gains. This alloy has a lower chromium and higher silicon content than JS-3 and New Crofer, which is probably the reason for the larger mass gain. At 800^{o}C, JS-3 and New Crofer seem to be best suited for use as interconnects. Both alloys form a protective manganese chromate layer. Also, compared to the other alloys at this temperature, JS-3 and New Crofer have small amounts of internal alumina and silica formation.

At 900^{o}C, the mass gains varied from about 0.68 mg/cm^2 for 26 Cr Ferritic in air + 0.1 atm H_2O to 5.16 mg/cm^2 for ZMG232 in dry air after only 501 hours. The 26 Cr Ferritic alloy is at the low range of the mass change data. This alloy forms a manganese chromate layer, but this layer has spalled in some areas. Vaporization of chromia, due to the lack of a continuous manganese chromate layer, is responsible for the low weight gains. AL453 is at the upper range of mass change data. It is possible that the relatively large amount of silicon and aluminum in this alloy is responsible for this. Also, the extent to which aluminum internally oxidized in the three environments studied could lead to a greater increase in mass for this alloy over the others. At 900^{o}C, Crofer and ZMG232 appear to be best suited for use in fuel cells. This is because when compared to other alloys at the same temperature, there is a small amount of alumina and silica that has formed beneath the surface. Also, Crofer and ZMG232 both form a manganese chromate layer above the chromia scale.

Analysis of the XRD pattern from a 26 Cr Ferritic sample proved that the sigma phase formed in the E-brite and 26 Cr Ferritic samples at 700^{o}C. The sigma phase formed more readily in 26 Cr Ferritic than in E-brite. The 26 Cr Ferritic alloy contains 2.2% molybdenum and silicon and E-brite contains 1.2% molybdenum and silicon. These elements increase the rate of sigma phase formation, and it is because 26 Cr Ferritic contains more of these elements than E-brite that the sigma phase forms more extensively in 26 Cr Ferritic.

The ASR values obtained from the conductivity experiments were all larger than the required value of 0.01 ohm cm^2. It was found that as the ASR decreases, the thicknesses of the oxides also tend to decrease.

A stress of -2.19 GPa was obtained from a Crofer sample exposed in dry air at 900^{o}C for 100 cycles. Crofer that had been exposed in air + 0.1 atm H_2O at 900^{o}C for 100 cycles had a stress of -2.06 GPa. These stress values can be compared to the calculated thermal stress for chromia (-2.22 GPa).

Alloys that have a high (but not too high) chromium content, low amounts of silicon and aluminum, and contain manganese and some reactive elements such as cerium or lanthanum have the best oxidation behavior for fuel cell applications.

BIBLIOGRAPHY

1. *Fuel Cell Handbook, Sixth Edition*. EG&G Technical Services, Inc., Morgantown, West Virginia, 2002.

2. “NFCRC: Fuel Cells Explained: What is and How does a Fuel Cell Work,” <http://www.nfcrc.uci.edu/fcresources/FCexplained/FC_howItWorks.htm>, Accessed on February 28, 2005.

3. Gindorf, Christian, Lorenz Singheiser, and Klaus Hilpert, “Chromium vaporization from Fe,Cr base alloys used as interconnect in fuel cells.” *Steel Research*, Vol. 72, No. 11 + 12, 2001, p. 528 – 533.

4. “Solid Oxide Fuel Cells,” <http://www.spice.or.jp/~fisher/sofc.html>, Accessed on February 28, 2005.

5. Perry, M. L. and T. F. Fuller, “A Historical Perspective of Fuel Cell Technology in the 20th Century.” *Journal of the Electrochemical Society*, Vol. 149, No. 7, 2002, p. S59 – S67.

6. “HFCIT Fuel Cells: Types of Fuel Cells,” <http://www.eere.energy.gov/hydrogenandfuelcells/fuelcells/fc_types.html?print>, Accessed on February 23, 2005.

7. “Fuel Cells 2000: Fuel Cell Basics: Applications,” <http://www.fuelcells.org/basics/apps.html>, Accessed on February 28, 2005.

8. Hilpert, K., W. J. Quadakkers, and L. Singheiser, “Interconnects.” *Handbook of Fuel Cells, Volume 4, Fuel Cell Technology and Applications: Part 2,* John Wiley & Sons Ltd., West Sussex, England, 2003, p. 1037 – 1054.

9. *Crofer 22 APU, Material Data Sheet No. 8005, June 2004 Edition*. ThyssenKrupp VDM, 2004.

10. “Materials Progress.” *Advanced Materials and Processes*, Vol. 162, No. 6, 2004, p. 19 – 20.

11. Quadakkers, W. J., J. Piron-Abellan, and V. Shemet, “Metallic Materials in Solid Oxide Fuel Cells.” *Materials Research*, Vol. 7, No. 1, 2004, p. 1 – 6.

12. Huczkowski, P., N. Christiansen, V. Shemet, J. Piron-Abellan, L. Singheiser, W. J. Quadakkers, “Oxidation Induced Lifetime Limits of Chromia Forming Ferritic Interconnector Steels.” Draft of article to appear in *Journal of Fuel Cell Science and Technology*, 2004.

13. *E-brite Alloy for Solid Oxide Fuel Cells, Technical Data Blue Sheet*. Allegheny Ludlum, 2002.

14. “Allegheny Rodney: An Allegheny Technologies Company,” <http:www.alleghenyrodney.com/pages/products/t446.asp>, Accessed on May 23, 2005.

15. *Stainless Steel AL 453 Alloy, Technical Data Blue Sheet*. Allegheny Ludlum, 2000.

16. Rakowski, James. Letter to G. H. Meier. October 28, 2003.

17. Rakowski, James. “RE: AL453 processing.” E-mail to the author. April 25, 2005.

18. “Hitachi Metals, Ltd. – Products – Automotive – Fuel Cell Materials,” <http://www.hitachi-metals.co.jp/e/prod/prod06/p06_15.html>, Hitachi Metals, Ltd., 2002, Accessed on March 21, 2005.

19. Horita, Teruhisa, Yueping Xiong, Katsuhiko Yamaji, Natsuko Sakai, Harumi Yokokawa, “Stability of Fe-Cr alloy interconnects under CH_4-H_2O atmosphere for SOFCs.” *Journal of Power Sources*, Vol. 118, 2003, p. 35 – 43.

20. Flinn, Richard A. and Paul K. Trojan, *Engineering Materials and Their Application, Second Edition*. Houghton Mifflin Company, Boston, 1981.

21. Smith, William F., *Structure and Properties of Engineering Alloys, Second Edition*. McGraw-Hill, Inc., New York, 1993.

22. “Stainless Steel – AISI 304 – Goodfellow, online source, sources, small quantity, quantities,” <http://www.goodfellow.com/csp/active/static/A/Stainless_Steel_-_AISI_304.HTML>, Accessed on April 19, 2005.

23. *Stainless Steels – Chromium-Nickel Types 302 (S30200), 304 (S30400), 304L (S30403), 305 (S30500), Technical Data Blue Sheet*. Allegheny Ludlum, 1998.

24. Bever, Michael B., ed., “Oxidation of Metals and Alloys.” *Encyclopedia of Materials Science and Engineering, Volume 5,* The MIT Press, Cambridge, Massachusetts, 1986, p. 3355 – 3360.

25. Birks, N., G. H. Meier, and F. S. Pettit, *Introduction to High Temperature Oxidation of Metals, Second Edition*, Unpublished Manuscript.

26. Birchenall, C. E., “Oxidation of Alloys.” *Oxidation of Metals and Alloys – 1970 Seminar*, ASM International, Materials Park, Ohio, 1971, p. 177 – 200.

27. Vander Voort, George F., “Embrittlement of Steels.” *ASM Handbook, Volume 1, Properties and Selection: Irons, Steels, and High-Performance Alloys, Tenth Edition*, ASM International, Materials Park, Ohio, 1990, p. 689 – 736.

28. Yang, Zhenguo, Matthew S. Walker, Prabhakar Singh, and Jeff W. Stevenson, “Anomalous Corrosion Behavior of Stainless Steels under SOFC Interconnect Exposure Conditions.” *Electrochemical and Solid-State Letters*, Vol. 6, No. 10, 2003, p. B35 – B37.

29. Yang, Zhenguo, Matthew S. Walker, Prabhakar Singh, Jeffry W. Stevenson, and Truls Norby, “Oxidation Behavior of Ferritic Stainless Steels under SOFC Interconnect Exposure Conditions.” *Journal of the Electrochemical Society*, Vol. 151, No. 12, 2004, p. B669 – B678.

30. Sarioglu, C., M. J. Stiger, J. R. Blachere, R. Janakiraman, E. Schumann, A. Ashary, F. S. Pettit, and G. H. Meier, “The adhesion of alumina films to metallic alloys and coatings.” *Materials and Corrosion,* Vol. 51, 2000, p. 1 – 15.

31. Coyne, Kelly, “Oxidation of Chromia Forming Materials for Interconnects in Solid Oxide Fuel Cells.” Senior Project, University of Pittsburgh, 2003.

32. Pettit, Frederick S., and Gerald H. Meier, “Volume I – Fundamental Studies of the Durability of Materials for Interconnects in Solid Oxide Fuel Cells, Phase I Topical Report, 1 October, 2002 – 31 May, 2003.” Report Date: 30 June, 2003.

33. Stott, F. H., and G. C. Wood, “Internal Oxidation.” *Materials Science and Technology*, Vol. 4, 1988, p. 1072 – 1078.

34. Guruswamy, S., S. M. Park, J. P. Hirth, and R. A. Rapp, “Internal Oxidation of Ag-In Alloys: Stress Relief and the Influence of Imposed Strain.” *Oxidation of Metals*, Vol. 26, Nos. 1/2, 1986, p. 77 – 100.